The rupture process of the MJ=7.2 1995 Hyogo-ken Nanbu (Kobe) earthquake deduced from S-wave polarization analysis

M.-P Bouin, M. Cocco, G. Cultrera, H Sekiguchi, K Irikura

Geophys. J. Int. (2000) **143,** 521–544

The rupture process of the $M_J = 7.2$ 1995 Hyogo-ken Nanbu (Kobe) earthquake deduced from *S*-wave polarization analysis

M.-P. Bouin,[1,*] M. Cocco,[1] G. Cultrera,[1] H. Sekiguchi[2] and K. Irikura[2]

[1] *Istituto Nazionale di Geofisica (ING), Via di Vigna Murata* 605, 00143, *Rome, Italy*
[2] *Disaster Prevention Research Institute, Kyoto University, Japan*

Accepted 2000 April 14. Received 1999 December 10; in original form 1998 December 6

SUMMARY

The use of *S*-wave polarization analysis for constraining high-frequency (>1 Hz) source parameters of large earthquake has been previously illustrated by Bouin & Bernard (1994) and Guatteri & Cocco (1996). In this paper, we show the efficiency of such a methodology applied to a data set in the presence of strong non-linear and liquefaction effects for the particular case of the 1995 Hyogo-ken Nanbu (Kobe) earthquake. The 11 strong-motion recordings from the closest stations to the fault plane have been analysed in the 0.6–2.0 Hz frequency band. We first correct the recorded ground motion data for the effect of shallow crustal anisotropy in the Kobe area, which allows us to remove part of the complexity of the observed *S*-wave polarigrams. Our results in terms of anisotropy parameters are in good agreement with those of previous studies performed in the same area. They show evidence, far from the faults, of a fast *S*-wave polarization oriented nearly parallel to the regional compressive stress direction, and, close to the faults, of a fast *S*-wave polarization oriented parallel to the faults' strikes. The corrected *S*-wave polarigrams are then interpreted in terms of rupture propagation along an extended fault. We consider three different faulting mechanisms: a pure right-lateral mechanism and two mechanisms with 30 and 50 per cent reverse components. The polarization data and the triggering times at the selected stations allow the identification of a set of subsources, demonstrating the need for a reverse slip component during the rupture of the two high-frequency (2.0 Hz) subevents on the Kobe fault section. The resulting locations of the main subevents in space and time provided an interval of possible values of rupture velocity ranging between 2.65 km s^{-1} (that is, 80 per cent of the shear wave velocity) and 3.46 km s^{-1} (that is, the value of the shear wave velocity). This study emphasizes that *S*-wave polarization can be a useful tool to restrict the number of reliable starting models for iterative waveform inversions.

Key words: earthquake source mechanism, polarization, *S* waves, strong ground motion.

1 INTRODUCTION

The rupture process of large earthquakes is currently investigated by inverting ground motion waveforms in a frequency bandwidth ranging between 0.1 and 2 Hz. Slip and rupture time distributions on the fault plane are retrieved by means of linear or non-linear (iterative) inversion procedures. The main limitations to the application of waveform inversion procedures are the trade-off between slip and rupture times (Spudich & Frazer 1984; Bernard & Madariaga 1984) and that between source and medium parameters due both to the incompleteness of the data set (poor azimuthal and distance coverage of the source) and to the inadequate modelling of unknown path effects. These limitations are manifest in the difficulty in imaging variable rupture velocity models: despite the heterogeneity of slip distributions, rupture velocities imaged for the most recent large-magnitude earthquakes are nearly constant [see Beroza (1991) and Wald *et al.* (1991) for the 1989 Loma Prieta earthquake, Wald & Heaton (1994) and Cohee & Beroza (1994) for the 1992 Landers earthquake, Wald *et al.* (1996) for the 1994 Northridge earthquake and Wald (1996), Yoshida *et al.* (1996) and Sekiguchi *et al.* (1996) for the 1995 Hyogo-ken Nanbu (Kobe) earthquake]. Moreover, deterministic modelling of ground motion waveforms is not easily applicable to high-frequency ($f > 2.0$ Hz) seismic waves.

* Also at: Département de Sismologie, UMR CNRS 7580, IPGP, France. E-mail: bouin@ipgp.jussieu.fr

An alternative approach to interpreting high-frequency seismic records is to analyse the *S*-wave polarization, which allows the simultaneous modelling of the horizontal components of ground motion. Previous studies (see e.g. Bernard & Zollo 1989) have demonstrated that, for a given distance and frequency range, the *S*-wave polarization angle is a more reliable and stable parameter than amplitude and phase. The main limitations consist of accounting for the effects of the free surface, which controls the distance (*S* window) and the frequency range (Nuttli 1961; Booth & Crampin 1985), and for low-velocity shallow layers (Bernard & Zollo 1989). Numerous studies have demonstrated the utility and the applicability of near-source *S*-wave polarization analyses for constraining earthquake source parameters (e.g. Bernard & Zollo 1989; Zollo & Bernard 1989; Capuano *et al.* 1994; Cocco *et al.* 1997) provided that possible anisotropy effects are correctly taken into account (Zollo & Bernard 1989; De Chabalier *et al.* 1992). Nevertheless, most of the applications of this method are restricted to seismic sources with dimensions much smaller than the source-to-receiver distance. Recently, Bouin & Bernard (1994) and Guatteri & Cocco (1996) applied the *S*-wave polarization analysis to the study of earthquake rupture processes on extended faults. Their approach was based on two simple assumptions: the use of the isochrone method (Bernard & Madariaga 1984; Spudich & Frazer 1984) and the validity of the near-source approximation, which implies that the wavelengths considered are shorter than the distance to the recording sites and shorter than the extended source dimension. Bouin & Bernard (1994) retrieved the details of the faulting process associated with the 1979 Imperial Valley (California, $M=6.7$) earthquake. Guatteri & Cocco (1996) verified the existence of slip partitioning during the 1989 Loma Prieta earthquake by analysing the *S*-wave polarization from local accelerograms. In the present paper, we aim to image the high-frequency rupture process of the well-studied 1996 January 16 (20:47 GMT) Hyogo-ken Nanbu (Kobe) earthquake using near-source *S*-wave polarization analysis.

A reliable image of the activated fault geometry of the Kobe earthquake was inferred from the aftershock distribution, geodetic displacement and surface breakage. The aftershock area (Hirata *et al.* 1996; Nakamura & Ando 1996) extends in a NE direction over a distance of about 50 km from the NW shore of Awaji Island to the NE edge of Kobe city (see Fig. 1). The geometry of the aftershock area coincides well with the distribution of the Quaternary faults previously mapped (Huzita & Kazama 1983), the Awaji and Kobe fault systems that mark the NW edge of the Osaka bay Plioquaternary basin. The main-shock hypocentre is located under the Rokko range between these two fault systems (see Figs 1 and 2), which separates the Kobe side from the Awaji side, suggesting bilateral faulting. In the Kobe area, the aftershocks are distributed along a plane striking nearly N50°E and almost vertical. In the Awaji area, the aftershock zone is more diffuse and extends in the N45° direction, dipping 75°–80°SE, as confirmed by geodetic data (Hashimoto *et al.* 1996). The main-shock focal mechanism (see Fig. 1) deduced from teleseismic records (Kikuchi & Kanamori 1996) is in good agreement with the surface observations and

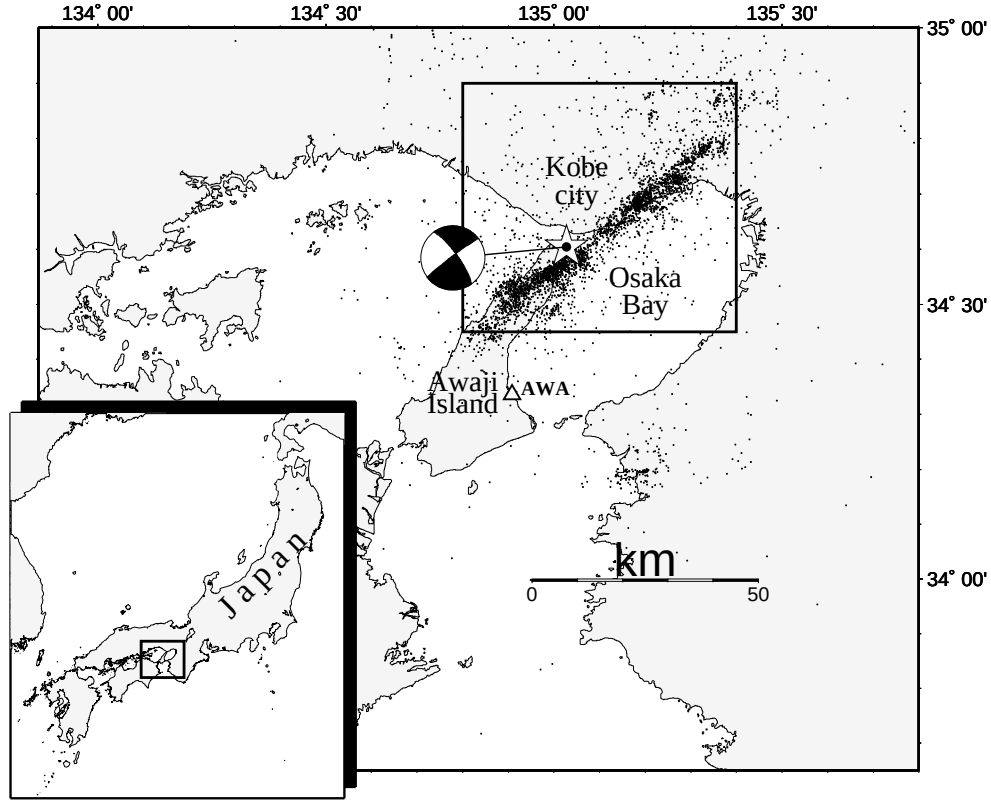

Figure 1. Main-shock location and aftershock distribution of the 1995 January 16 Hyogo-ken Nanbu (Kobe) earthquake. A map of the active faults in the area (Huzita & Kazama 1983) is shown in the figure. The star indicates the epicentre determined by JMA (1996) and the fault plane solution is the Harvard CMT mechanism. Aftershocks shown on the map (Hirata *et al.* 1996; Nakamura & Ando 1996) were recorded during the period 1995 January 17–February 23. The area delimited by the rectangle corresponds to the area of study (see Fig. 2). The open rectangle shows the position of the AWA recording site.

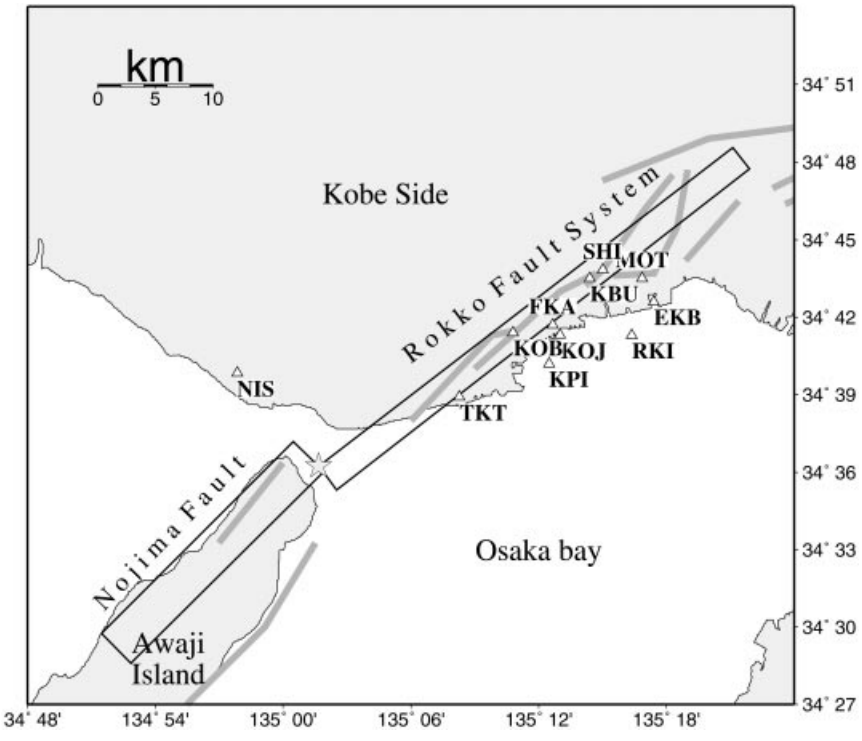

Figure 2. Distribution of the 11 selected strong-motion stations used in this analysis and the main active faults (Huzita & Kazama 1983). The star represents the hypocentre location (JMA 1996) and the rectangles depict the geometry of the theoretical faults used in this study.

the seismicity at depth. It shows a nearly right-lateral mechanism on a NE–SW-trending almost vertical fault, although a subevent with a larger reverse component is required to fit the teleseismic data (see Kikuchi & Kanamori 1996 for details). The leveling changes along the Himej–Osaka route (see Hashimoto *et al.* 1996) on the Kobe side clearly require uplift of the NW side of the fault relative to the SE.

Fig. 2 summarizes the geometry of the theoretical faults assumed by most of the authors to fit ground motion waveforms as well as geodetic data. In the present study we refer to the Suma, Suwayama and Gosukebashi faults as the Rokko fault system. Near-source strong-motions, teleseismic body waveforms and geodetic displacements have been inverted independently (Hashimoto *et al.* 1996; Ide & Takeo 1996, Kikuchi & Kanamori 1996; Sekiguchi *et al.* 1996) and jointly (Wald 1995, 1996; Horikawa *et al.* 1996; Yoshida *et al.* 1996) to determine the spatial and temporal dislocation pattern on the fault plane. Three main slip patches were imaged (see Horikawa

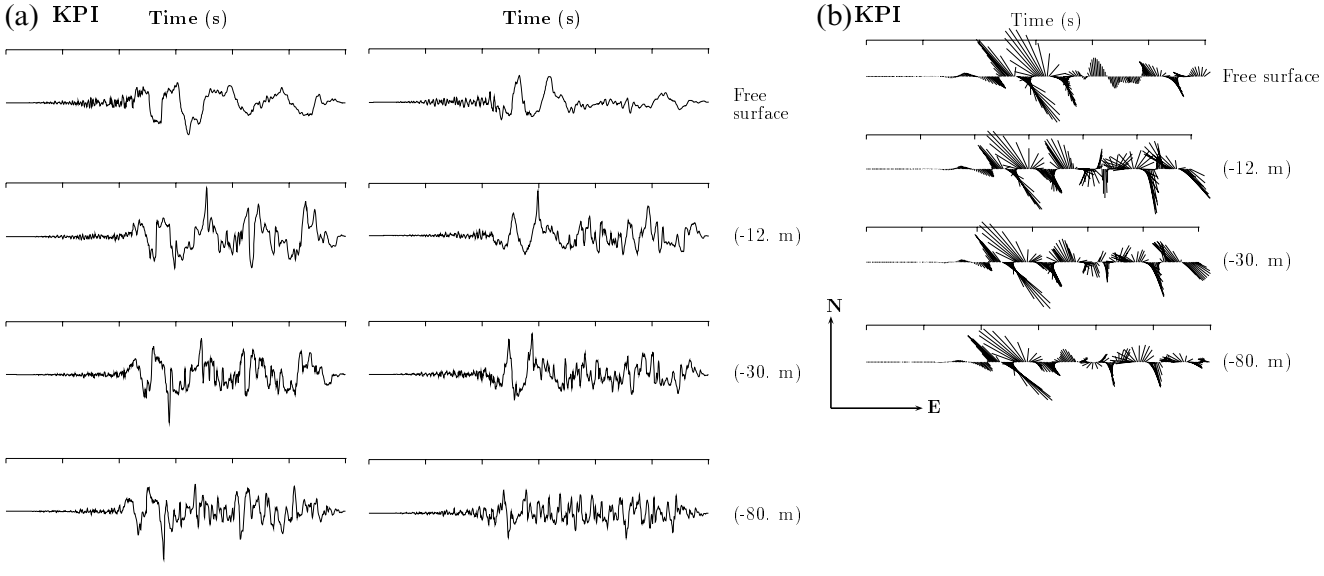

Figure 3. (a) Horizontal components of the raw acceleration recorded at different depths at the KPI borehole. The time increment is 1 s. Depth is indicated on the right side of the figure. Left panel: N–S component; right panel: E–W component. (b) Horizontal polarization versus time in the NE plane of the integrated acceleration, bandpass filtered within 0.6 and 2.0 Hz, recorded at different depths at the KPI borehole. The time increment is 1 s. Depth is indicated on the right side of the figure.

Table 1. Strong-motion stations.

Station	Lat. (°N)	Long. (°E)	Owner	Data format*	Sampling rate Hz
KBU	34.725	135.240	CEO	vel	100
MOT	34.725	135.281	CEO	vel	100
KOJ	34.6685	135.217	PHR	acc	100
SHI	34.7306	135.250	K. Elec.	acc	250
KPI	34.670	135.208	K. city	acc	100
FKA†	34.695	135.211	O. g.	acc	100
EKB	34.71	135.29	PWRI	acc	100
TKT	34.6485	135.138	JR	acc	100
KOB	34.69	135.18	JMA	acc	50
NIS	34.664	134.964	JR	acc	100
RKI	34.6883	135.2728	Sek. H.	acc	100
AWA	34.336	134.908	JMA	acc	20

* acc: acceleration, vel: velocity
† only horizontal components
K. city: Kobe City; CEO: Committee of Earthquake Observation and Research in the Kansai Area, CEORKA, O. g.: Osaka Gas, JMA: Japan Meteorological Agency, K. Elec.: Kansai Electric Power Co. Inc., PHR: Port and Harbor Research Institute, JR: Japan Railway Institute, Sek. H.: Sekisui House Co. Inc., PWRI: Public Works Research Institute Ministry of Construction.

et al. 1996; Ide & Takeo 1996; Kakehi *et al.* 1996; Sekiguchi *et al.* 1996; Wald 1996; Yoshida *et al.* 1996): the first is located near the hypocentre (at roughly 16 km depth) on the fault plane beneath Kobe; the second is located at shallow depths on the Nojima fault on Awaji island (where surface breakages were also observed; see e.g. Nakata & Yomogida 1995); the third is located roughly 20 km NE of the hypocentre on the Kobe fault system. Hereafter we refer to the two subevents on the Kobe fault system as the first and third subevents, maintaining their temporal sequence. The total rupture duration was nearly 12 s (Ide & Takeo 1996; Sekiguchi *et al.* 1996; Wald 1996; Yoshida *et al.* 1996). The largest slip amplitudes range between 2.5 and 3 m and were located on the Nojima fault. The first slip patch (the closest to the hypocentre) below the Kobe area is larger and deeper than the third one, and is characterized by a dominant reverse slip component. An important feature common to all of the results summarized is the strong heterogeneity of slip distribution and the spatial variation of the slip direction (the rake angle) during faulting.

2 DATA PROCESSING

For the present study, we have selected the 11 closest strong-motion sites located at distances of less than 10 km from the fault trace (see Table 1 and Fig. 2). We analyse the recorded waveforms in the 0.6–2.0 Hz frequency bandwidth, which contains most of the power of the velocity spectra and can be modelled with the far-field approximation (see Farra *et al.* 1986). We first process the recorded time histories to obtain ground velocities and therefore we correct the waveforms to remove most of the perturbing anisotropy effects at high frequencies. We interpret the corrected polarigrams in order to locate the areas of high energy release and constrain the rupture velocity and the direction of slip during faulting.

2.1 Ground motion records

Ground motion data were provided by the Committee of Earthquake Observation and Research in the Kansai Area (CEORKA), the Japan Meteorological Agency (JMA), Kansai Electricity Power Co. Inc., the Port and Harbor Research Institute, the Japan Railway Institute (Nakamura 1995; Nakamura *et al.* 1996), Sekisui House Co Inc., the Public Works Research Institute Ministry of Construction, Osaka Gas and Kobe city. The original data at KBU and MOT were clipped in some components. Kagawa *et al.* (1996) revised those seismograms based on the saturation characteristics of the sensor. The common frequency domain in which the frequency response is flat for all the sensors corresponding to the selected records ranges from 0.1 to 7 Hz.

Table 2. Trigger times (trigger time of the station-origin time of the event).

Station	*P* waves T_p (s)	T_a (s)	δ_t (s)	*S* waves T_p (s)	T_a (s)	δ_t (s)	T_t (s)	Δt_p (s)	Δt_s (s)
NIS	3.39	2.14	+1.25	5.87	4.39	+1.48			−0.23
TKT	3.60			6.24	2.13	+4.11			
KOB	4.21	28.56	−24.35	7.3	32.06	−24.76	−24.5	−0.15	0.26
KPI	4.35	9.37	−5.02	7.54	13.25	−5.71	−4.76	0.26	0.95
KOJ	4.56			7.9	2.75	+5.15			
FKA	4.54	4.01	+0.53	7.87	7.62	+0.25			0.28
KBU	5.08	27.82	−22.74	8.8	31.28	−22.48	−22.82	−0.08	−0.34
SHI	5.241	6.66	−1.42	9.07	10.44	−1.37			−0.05
RKI	5.18	9.53	−4.35	8.97	14.08	−5.11			0.76
EKB	5.25	0.36	+4.95	9.56	4.66	+4.9			0.05
MOT	5.53	29.43	−23.9	9.57	33.5	−23.93	−23.72	0.18	0.21

T_p: theoretical propagation time
T_a: arrival time measured on the row data
$\delta_t = T_p - T_a$: Observed trigger time
T_t: absolute trigger time when available
Δt_p: time delay between the absolute trigger time when available and the observed trigger time from *P* waves
Δt_s: time delay between the trigger time, absolute when available or observed from *P* waves, and the observed trigger time from *S* waves
Hypocentre (JMA): 34.604°N, 135.0276°E, depth = 17.7 km, 17:46:51.5 JMT (Nemoto *et al.* 1997)

For polarization studies, a first point to check in the data is the correctness of the instrument orientations. We have verified the recording orientations by comparing the ground motion time histories displayed in the report on strong-motion records of the 1995 Hyogo-ken Nanbu earthquake (Special Working Group of the 1995 Hyogo-ken Nanbu earthquake 1996) with our digital waveforms. Ground velocities were obtained by integrating the recorded accelerograms or by filtering the velocity records (depending on the sensor characteristics; see Table 1). Because polarization analyses require no phase distortion, we used a zero-phase filter. The selected frequency bandwidth (0.6–2.0 Hz) contains most of the power of the velocity spectra and allows us to avoid the contribution of near-field terms and to reduce the effects of local site geology. At lower frequencies ($f<0.6$ Hz), the far-field approximation would be inadequate for several propagation paths. At higher frequencies ($f>2$ Hz), non-linear and liquefaction effects reduce significantly the ground motion amplitudes (see Aguirre & Irikura 1995). This is evident in Fig. 3, where we compare the horizontal components of the unfiltered ground acceleration recorded at KPI on four borehole sensors located at different depths (Fig. 3a) with the horizontal polarization of the integrated acceleration, bandpass filtered in the selected bandwidth (Fig. 3b). This figure clearly shows that ground velocity time histories filtered in the 0.6–2.0 Hz frequency band allow the analysis of coherent signals.

Because the absolute times are available only for few of the selected seismic stations, we have computed the theoretical triggering times (see Cocco & Pacor 1993 for details of this calculation) using the hypocentral location and the origin time provided by the Japan Meteorological Agency (JMA: 34.604°N, 135.0276°E, depth 17.7 km, 20:46:51.5 01/16/1995 GMT), reading the *P* and *S* first arrivals on the recorded waveforms and calculating the theoretical arrival times using the velocity model proposed by Sekiguchi *et al.* (1996) for the KBU site (which does not differ considerably from the rock site velocity model used by Wald 1996 and other authors). The resulting triggering times are listed in Table 2 together with the absolute times (when available) and the time delay between theoretical and observed *P* and *S* arrival times.

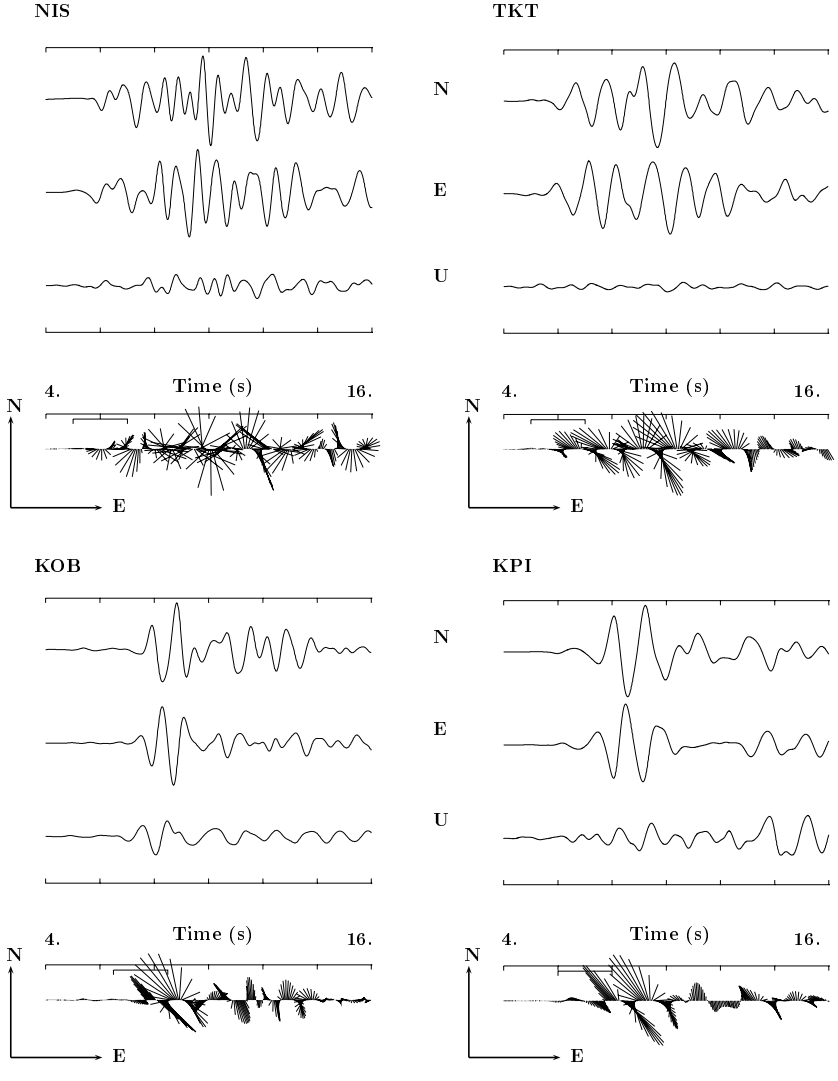

Figure 4. Time histories of ground velocity (north, east and up) bandpass filtered between 0.6 and 2 Hz, and horizontal polarization versus time in the NE plane (polarigram). The time window used for the correction from anisotropy (see Table 3) is indicated under the time axis of the polarigram. The recordings are corrected for the trigger time (absolute or theoretical) listed in Table 2 (see text).

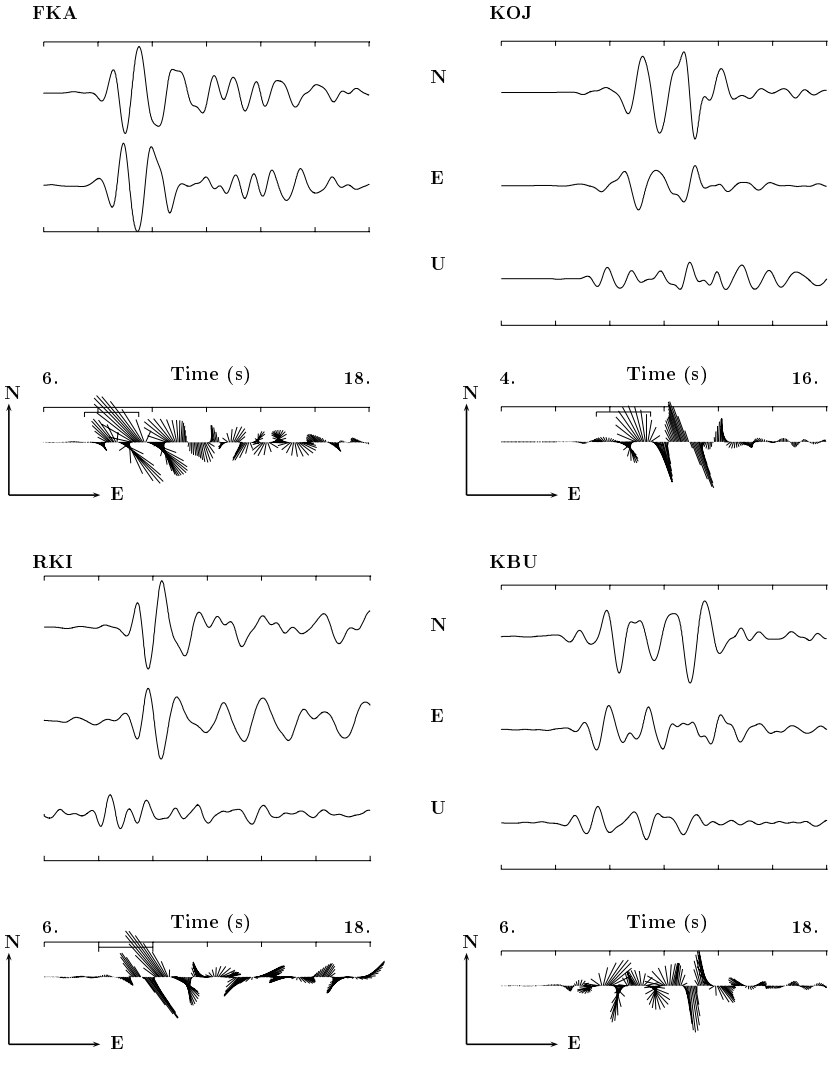

Figure 4. (*Continued.*)

2.2 *S*-wave polarization analysis

Fig. 4 shows the three components of ground velocity used in this study bandpass filtered between 0.6 and 2.0 Hz together with the corresponding polarization vectors of the horizontal velocity plotted as a function of time. The recordings have been corrected for the triggering time (listed in Table 2). The vertical component of the FKA station is not available. The stability of the *S*-wave polarization at KOB, KPI, FKA, RKI and EKB is quite striking, while at the other sites (NIS, TKT, SHI, KOJ, MOT and KBU) the first seconds of the *S* phases show a variable polarization of the velocity vector related to an elliptical horizontal motion.

Following Zollo & Bernard (1989) and Bouin *et al.* (1996), we adopted a selection criterion for the available data set in order to eliminate scattered or converted phases: we selected the waveforms for which the amplitudes on the vertical component at the time of the direct *S* wave arrival are significantly smaller than those on the horizontal components. As shown in Fig. 4, an energetic phase arrives on the vertical components recorded at KBU and MOT just before the first cycle of *S* waves on the associated horizontal components. This phase perturbs the polarization of the direct *S* wave. For this reason, we exclude these data from the following analyses. Because the vertical component at the FKA station is not available, it is impossible to verify these records according to the criterion proposed above. Nevertheless, a scattered or converted phase is expected to give rise to an energetic vertical arrival that leads to a destabilization of the horizontal *S*-wave polarization, which is not observed on the FKA recordings. Consequently, we may reasonably assume that the FKA record matches the selection criterion. For the other sites, the amplitudes on the vertical component associated with the arrival of the *S* waves are significantly smaller or almost null (see Fig. 4). Thus, complex arrivals cannot explain the unstable *S*-wave polarization observed at NIS, TKT, KOJ and SHI, which we interpret in terms of upper crustal anisotropy.

2.3 Correction for crustal anisotropy

The existence of an anisotropic upper crust in the Kobe area was pointed out by Tadokoro *et al.* (1999) in their analysis of the Kobe aftershocks. They showed that for stations far from causative faults the direction of fast *S*-wave polarization is oriented nearly E–W, in agreement with the local stress direction in the frame of the EDA model (Crampin 1987). For

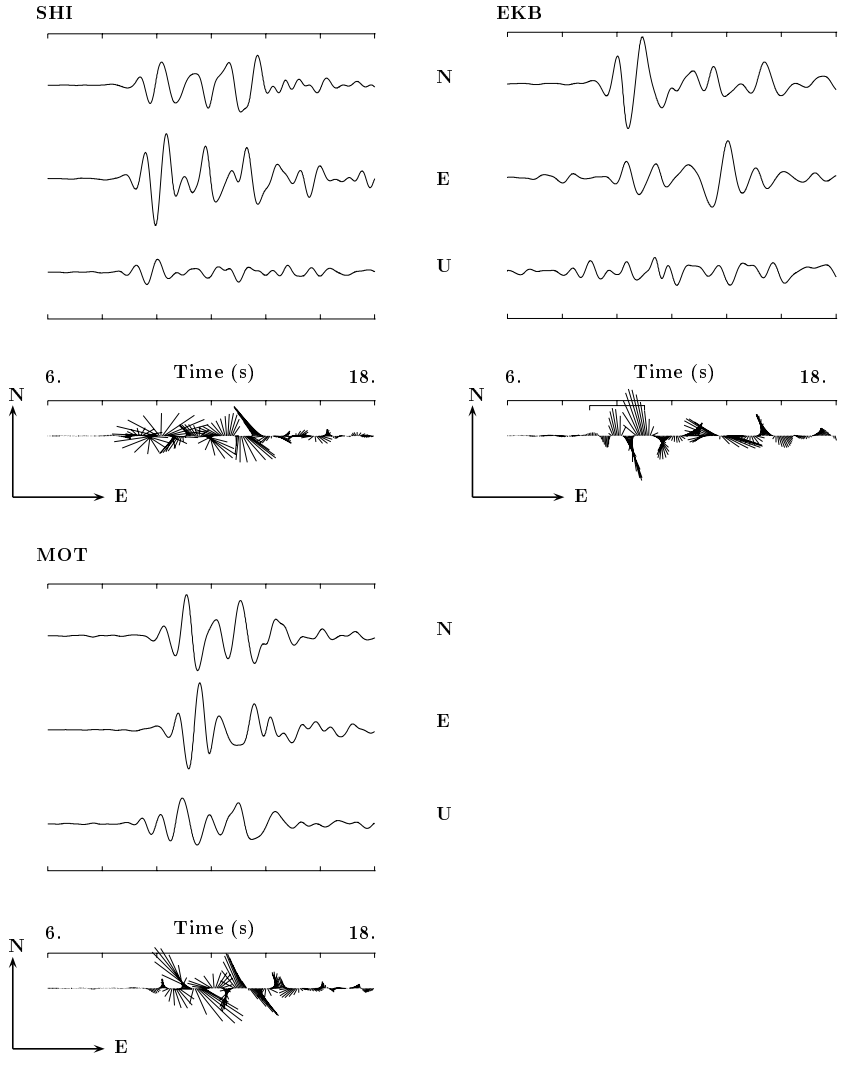

Figure 4. (*Continued.*)

stations installed very near active faults, the direction of the fast *S*-wave polarization is parallel to the strike of the fault (see e.g. Kaneshima 1990; Savage *et al.* 1990; Gledhill 1991; Zhang & Schwartz 1994; Zuniga *et al.* 1995; Evans *et al.* 1995; Bouin *et al.* 1996).

Based on these results, we will assume that anisotropy may have perturbed the *S* waves radiated during the main shock. The correction for the anisotropy effect is based on a well-known cross-correlation function technique first developed by Bowman & Ando (1987). In order to perform this correction, it is necessary to define a time window in which the two components are cross-correlated. We have chosen a relatively short time window of less than 2 cycles (see Table 3 and Fig. 4).

At FKA, KOB, KBU, EKB and KPI, the highest correlation is obtained for a zero delay between components, which is consistent with the clear stable polarization evident in the uncorrected data. This suggests either the absence of anisotropy under these sites, or a fast anisotropy axis oriented parallel or perpendicular to the recorded *S*-polarization vector. We cannot rule out any of these hypotheses without more information. For this reason, we report both directions (which are equally probable in our analysis) in Table 3 as well as the anisotropy parameters obtained for the other sites. Table 3 and Fig. 5 summarize our results, which are in agreement with those of previous studies. The interpretation of the data recorded at TKT requires special care. The N104°E direction of fast *S*-wave polarization that we have obtained from the analysis of the main-shock recordings is significantly different from the N54°E direction obtained at a very close temporary station (TKST) by Tadokoro *et al.* (1999). These authors analysed the records from six aftershocks, five of which were located below the station. For these five aftershocks the direction of fast *S*-wave polarization is very coherent and in a direction N54°E. Nevertheless, for the last aftershock, located in the hypocentral area, the fast *S*-wave polarization direction is significantly different, oriented nearly E–W, in agreement with the results that we obtained from the main-shock recordings (see Table 3).

The corrected polarigrams are plotted in Fig. 6. Comparison with Fig. 4 shows that, after correction, the *S*-wave polarization vector is more stable at stations TKT and NIS. The polarization resulting from the correction at SHI is still highly unstable. Moreover, the correlation peak is strongly dependent on the selected time window and the filtering procedure. This might be due to the inadequacy of the correction applied, as well as to source or propagation path effects. For those reasons, we will exclude this station from the following investigations.

Table 3. Correction of *S* splitting.

Station	Pol. of fast S* (°)	Δt† (s)	Max C.	Window (s)	
NIS	13.0	−0.15	0.95	5.0	7.0
TKT	14.0	−0.12	0.94	5.0	7.0
KPI‡	70.0 or 160.0	0.00		6.0	8.0
KOB‡	52.0 or 142.0	0.00		6.5	7.5
FKA‡	43.0 or 133.0	0.02		7.5	9.5
KOJ	16	−0.15	0.98	7.5	9.5
SHI					
RKI‡	103.0 or 193.0	0.00		8.0	10.0
EKB‡	103.0 or 193.	0.00		9.0	11.0
MOT					
KBU					

* Clockwise from North
† Time delay between fast and slow *S*
Max C.: maximum of the correlation function
‡ Or no anisotropy

A similar analysis performed in a higher-frequency bandwidth (1–3 Hz) led to similar results in terms of anisotropy parameters—the fast axis direction ($\pm 5°$) and time delay (± 0.04 s)—for all the other stations. This supports the validity of the correction applied.

3 INTERPRETATION OF CORRECTED POLARIGRAMS

The analysis of horizontal corrected polarigrams (Fig. 6) shows several interesting features. The *S*-wave polarization vector is stable for most of the signal duration (~ 5 s, see the light grey shaded area in Fig. 6). This is striking at TKT, KPI and FKA. This stability means that, for those stations, there were no variations of the *SV* and *SH* coefficients during the selected time window. This is quite a surprising result, because due to the proximity of the recording sites to the fault plane (see Fig. 2), the rupture propagation from the hypocentre to the receivers along the fault plane should produce a time variation of the *S*-wave polarization vector. Moreover, we observe an evident time variation of the *S*-wave polarization vector on the polarigrams at stations EKB and RKI as shown in Fig. 6 (dark grey shaded area). One may suggest that this late pulse, polarized in a different direction with respect to the first pulses, could be due to diffracted waves coming from the basin edge. However, we emphasize that a diffracted phase should have an energetic phase on the vertical component (Zollo & Bernard 1989): as shown in Fig. 4, this is clearly not observed in the data. Moreover, Irikura *et al.* (1996) have computed synthetic seismograms using a finite element 3-D code to account for the effects of the Osaka basin, whose geometry was reconstructed in detail. The analysis of the polarization resulting from those seismograms for receivers close to EKB and RKI indicates a polarization direction very different from those observed at the two sites. Therefore, we suggest that this phase is a direct *S* wave and we consider the temporal change of polarization observed at these two sites to be related to the rupture process.

Therefore, we believe that any acceptable source model should explain these two main observations: the direction, stability and duration of the *S*-wave polarization, which is oriented NNE–SSW at station NIS and NNW–SSE at the other stations selected (TKT, KOB, KPI, FKA, KOJ, RKI and EKB), and the temporal change in the *S*-wave polarization direction at sites RKI and EKB (see Fig. 6).

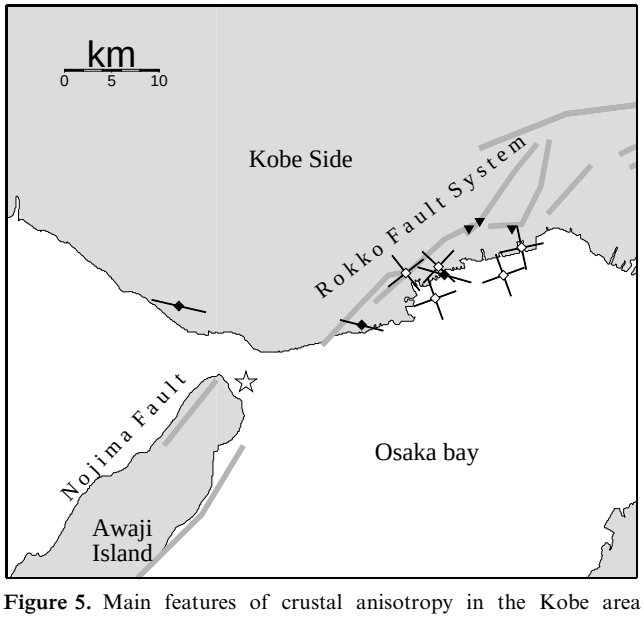

Figure 5. Main features of crustal anisotropy in the Kobe area inferred in this study (see Table 3) plotted on a map of active faults (Huzita & Kazama 1983). The segments centred on each station give the direction of the fast *S*-wave polarization. When two directions are equally probable, both are plotted. Solid triangles represent the stations excluded from *S*-wave polarization analysis (see text). The star represents the hypocentre location (JMA 1996).

4 EXPECTED *S*-WAVE POLARIZATION FROM AN EXTENDED SOURCE

The study of *S*-wave polarization radiated by extended sources requires a suitable approach, which we briefly explain in this section. The main advantage of polarization investigations, with respect to the separate modelling of different components of ground motion recordings, is the simultaneous fit of the two horizontal components and therefore a better control on the rupture mechanism (see e.g. Guatteri & Cocco 1996).

We compute synthetic seismograms using the isochrone approach (see Spudich & Frazer 1984 and Bernard & Madariaga 1984 for details of the theory). We adopt a source model for the 1995 Kobe earthquake deduced from the results presented by Wald (1996), Segikuchi *et al.* (1996) and Yoshida *et al.* (1996). We assume a single fault plane striking N50° and dipping 85°NW. The total length is 60 km, which also includes the Nojima fault to the south (20 km SE of the hypocentre). The fault plane is 20 km wide. These values agree well with the fault parameters adopted by most authors. In this first attempt, slip is uniformly distributed on the fault plane and its amplitude is chosen to fit the seismic moment ($M_o = 2.5 \times 10^{26}$ dyn cm). The slip direction is assumed to be a pure right-lateral mechanism (rake 180°). The rupture time distribution on the fault plane is shown in Fig. 7 (upper panel); we assume a constant rupture velocity equal to 2.8 km s^{-1}. Fig. 7 (middle panel) shows the isochrone distribution; the bottom panel shows the resulting theoretical *S*-wave polarization computed for station TKT. The larger gradient of the isochrones indicates the directivity and allows one to identify the zone that can radiate the larger ground motion amplitudes (Spudich & Frazer 1984). This figure

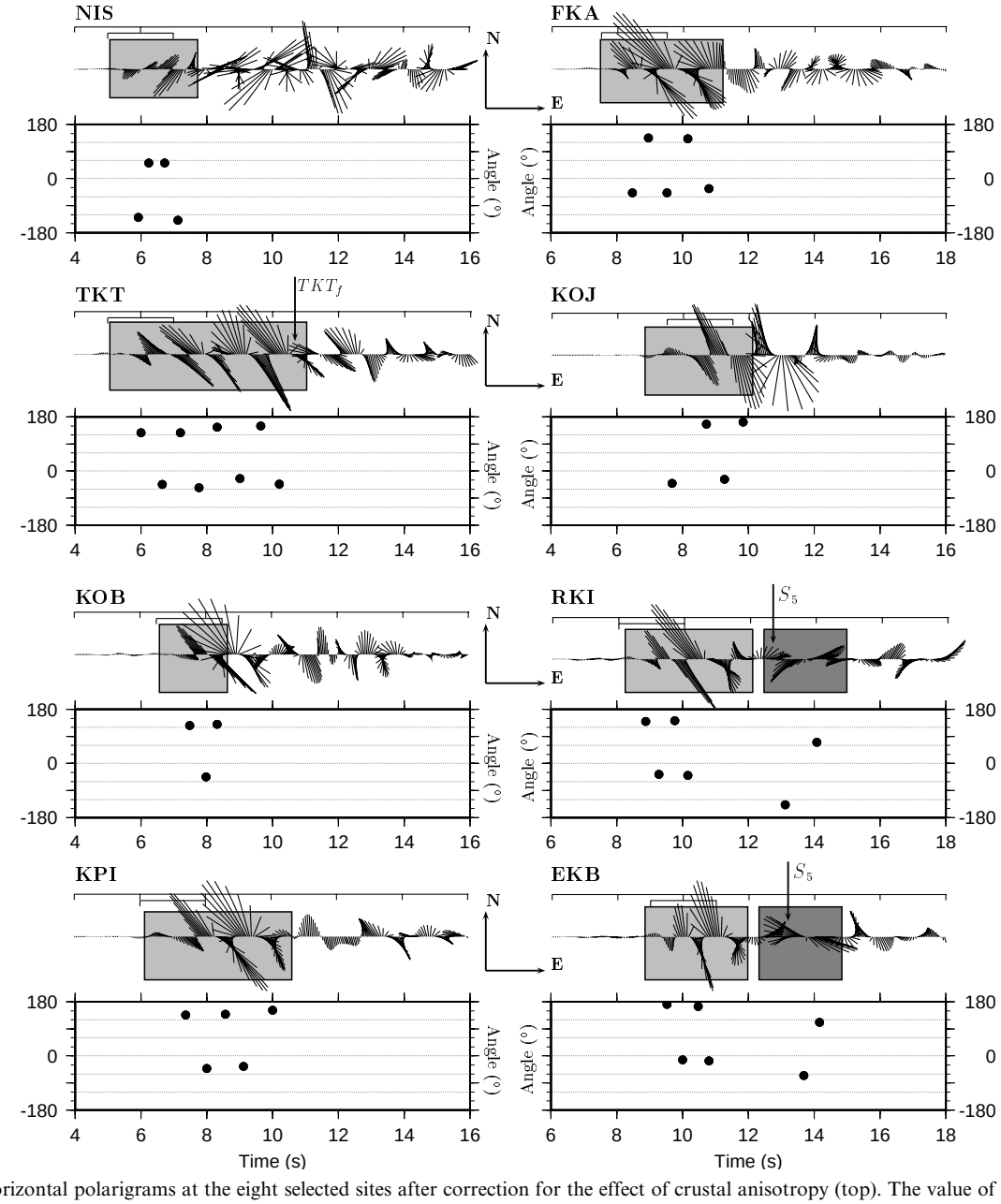

Figure 6. Horizontal polarigrams at the eight selected sites after correction for the effect of crustal anisotropy (top). The value of the polarization angle for the maximum amplitude of the pulses versus time is shown (bottom panel). The vertical arrows correspond to the arrival times of the different phases reported in Table 4 and discussed in the text. The light grey filled rectangles indicate the time windows where the *S*-wave polarization direction is stable. The dark grey filled rectangles (at stations RKI and EKB) depict the pulses whose the polarization direction is different from the former phases radiated by the rupture nucleation. The subevent radiating such pulses at RKI and EKB is named S_5 in the text.

shows that, for the assumed rupture model, the theoretical polarization expected at TKT is constant for most of the *S* time window and that the polarization changes suddenly when the rupture front is in a nodal position for the assumed faulting mechanism, that is, when the rupture front is passing close to the receiver. We refer to a constant *S*-wave polarization angle as stable polarization. The stability of the polarizations strongly depends on the distance of the recording site from the fault plane: the area where the rupture front is in a nodal position can be identified only for those receivers very close to the fault plane (such as TKT). At TKT the expected *S*-wave polarization is weakly dependent on the assumed rupture velocity (in the range 2.8–3.1 km s^{-1}). The rotation of the polarization direction is caused by sources located in the strike direction at the same distance from the hypocentre, indicating that we have no vertical resolution, as expected for a nearly vertical strike-slip fault and for the distribution of the selected recording sites (similar to a parallel array). Fig. 7 also shows that, despite the stability of the *S*-wave polarization, the largest amplitudes are radiated by the fault portion closest to the station, as also shown by the isochrone distribution.

The isochrone approach also allows us to image the area of the fault that is radiating most of the energy at a selected recording site. Following the approach proposed by Spudich & Oppenheimer (1986) and Guatteri & Cocco (1996), we can compute the radiated power as a function of the position on the

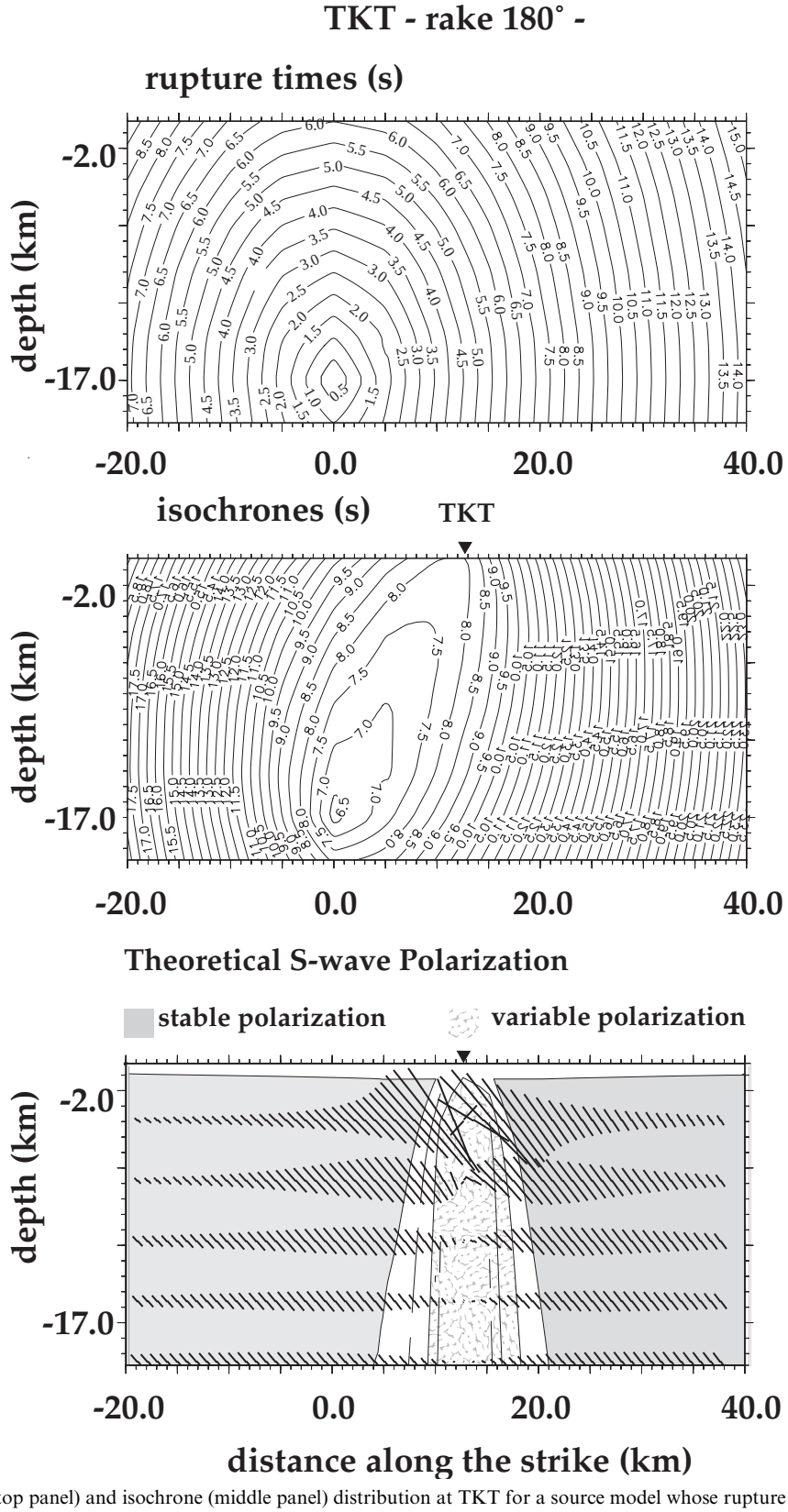

Figure 7. Rupture time (top panel) and isochrone (middle panel) distribution at TKT for a source model whose rupture velocity is 2.8 km s^{-1} and where the slip direction is a pure right-lateral mechanism (rake 180°). The fault geometry (strike 50°, dip 85°NW) and the position of rupture nucleation are taken from previous studies. The expected *S*-wave polarization is plotted in the bottom panel: the shaded areas indicate the fault portions that radiate a stable polarization at TKT; the stippled area shows the zone where the polarization vector rotates because the rupture front is in a nodal position with respect to the station position (indicated by the solid triangle). We also plot on the bottom panel the direction of the theoretical *S*-wave polarization vector radiated by each subsource at TKT projected in the NE plane (plane of the figure). The length of the vector is proportional to the relative amplitude.

fault plane for the rupture model described above and presented in Fig. 7 (uniform slip distribution). The results of these calculations are shown in Fig. 8, where we have grouped those stations having similar patterns. Despite the removal of the effect of the spatial distribution of slip over the entire fault surface, Fig. 8 shows that the radiation arriving at particular groups of stations is radiated non-uniformly from the fault. All the stations located NE of the epicentre cover almost the same fault section, while NIS receives seismic waves only from the hypocentral zone. EKB and RKI are the stations that better resolve the fault planes belonging to the NE edge of the Kobe fault system. It is important to point out that if we plot the isochrone curves responsible for the largest peak ground velocities for each station on the fault plane, they lie within the shaded areas shown in Fig. 8 (see Fig. 7 for TKT). Due to the distribution of the selected recording sites (see Fig. 2), the resolution on the Nojima fault is very low (only AWA, not used in our analysis, receives seismic waves radiated by that fault section), but it is quite good for the Rokko fault system in the Kobe area (see Fig. 8). For this reason, in the following we investigate the rupture process only on the Kobe fault section.

Figs 7 and 8 were computed under the assumption of a pure right-lateral mechanism. Because the direction of the slip vector (the rake angle) controls both the radiated power and the theoretical *S*-wave polarization, we computed the distribution on the fault plane of the radiated power and the theoretical *S*-wave polarization for rupture models having the same slip distribution and rupture velocity (shown in Fig. 7) but different values of the rake angle. We consider three different slip directions: a rake angle of 180°, which corresponds to a pure right-lateral mechanism as already described, and two oblique mechanisms with rake angles of 150° and 135° (we fix the upper limit of the reverse slip component to 135° in agreement with previous studies).

Our results show that the area that radiates the higher power to NIS does not change if different rakes are used, and also at EKB and RKI the distribution of the radiated power on the fault plane is modestly dependent on the slip direction. Fig. 9 shows the radiated power and the theoretical polarization at TKT resulting from the different source models. Increasing the reverse component of the slip vector modifies the resulting *S*-wave polarization pattern. First, the position of the nodal zone on the fault plane is moved along the strike towards the NE for increasing depths. Consequently, the area that radiates a stable polarization increases with depth. Second, the distribution of the radiated power on the fault plane changes with the assumed slip direction. Similar behaviour is observed for KBU, SHI, KOB, KOJ, KPI and FKA. These computations

Table 4. *S* arrival time delay after the origin time of the event.

Station	TKT_f (s)	S_5
TKT	10.72	
RKI		12.4
EKB		13.2

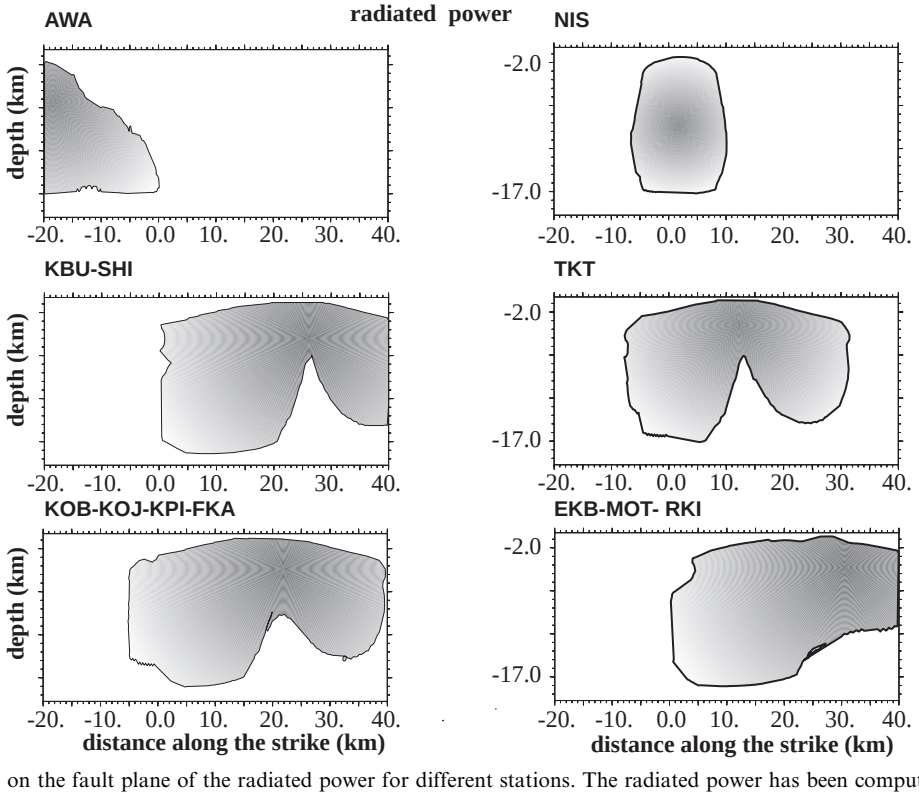

Figure 8. Distribution on the fault plane of the radiated power for different stations. The radiated power has been computed using the isochrone approach following the method proposed by Spudich & Oppenheimer (1986) and Guatteri & Cocco (1996) (see these papers for the equations). We plot the area where the radiated power is larger than zero (shaded areas); the shades of grey correspond to the spatial variation of the radiated power, which is maximum inside the shaded area and decreases at the border. We have grouped those stations having a similar pattern. This figure shows that the power is radiated non-uniformly, and that several stations receive contributions from the same portion of the fault plane.

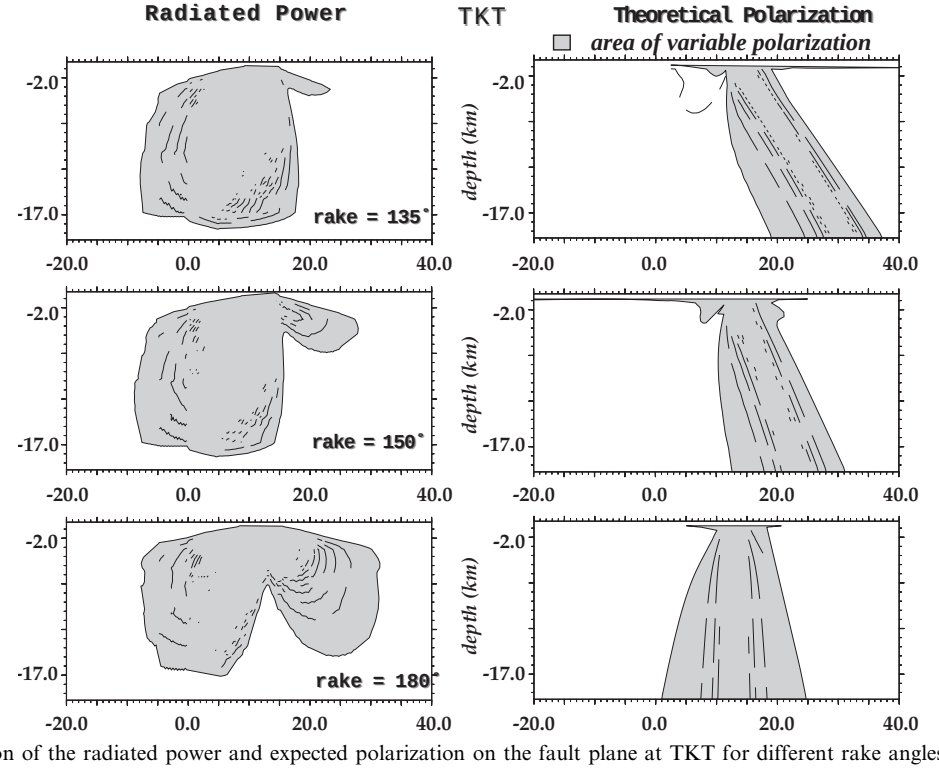

Figure 9. Distribution of the radiated power and expected polarization on the fault plane at TKT for different rake angles. The different source models have the same rupture time distribution and uniform slip on the fault but different slip directions. We plot the fault patches where the radiated power is different from zero (shaded areas on the left panels) as described in Fig. 8. We also show the areas of variable theoretical polarizations (shaded areas on the right panels): the white patches identify the portions where the expected polarization is stable (and oriented nearly perpendicular to the fault plane). Inside the shaded areas we drawn the change of *S*-wave polarization direction (contour level is 5°). This emphasizes that the position of the nodal zone on the fault plane depends on the assumed slip direction.

Table 5. Mean rupture velocity.

	Pure strike slip			30 per cent reverse slip			50 per cent reverse slip		
Depth (km)	Dist* (km)	T_n (s)	V_r (km s^{-1})	Dist* (km)	T_n (s)	V_r (km s^{-1})	Dist* (km)	T_n (s)	V_r (km s^{-1})
8	21	9.85	2.34	23.5	10.08	2.52	25	10.1	2.65
12	21	8.8	2.45	26	9.02	2.95			
16	21	7.8	2.7						
20	21	6.69	3.15						

* Distance from vertical line passing hypocentre
T_n: nucleation time of the S_5 source
V_r: rupture velocity ± 0.36 km s^{-1}

Table 6. S_5 phase theoretical arrival time delay after the origin time of the event.

Station	Pure strike slip				30 per cent reverse slip		50 per cent reverse slip	
	8 km	12 km	16 km	20 km	8 km	12 km	8 km	12 km
NIS	17.108	16.604	16.272	15.704	18.522	18.867	19.216	18.617
TKT	13.675	12.825	13.310	13.146	14.981	15.021	15.644	14.771
KPI	12.685	12.294	12.628	12.606	13.615	13.488	14.112	13.238
KOB	12.662	12.181	12.578	12.549	13.656	13.544	14.184	13.294
FKA	12.419	12.297	12.453	12.457	13.186	12.999	13.613	12.749
KOJ	12.452	12.324	12.483	12.485	13.219	13.036	13.642	12.786
SHI	12.427	13.214	12.556	12.533	12.552	12.418	12.623	12.168
MOT	12.657	13.677	12.773	12.719	12.557	12.542	12.458	12.292
KBU	12.361	12.968	12.485	12.477	12.635	12.458	12.801	12.208

demonstrate that the propagation of the rupture front and the direction of the slip vector affect the expected *S*-wave polarization at a particular recording site for a given source-to-receiver geometry.

5 MODELLING THE RUPTURE HISTORY

In the first step of our investigation we try to identify the high-frequency subsources that radiated the observed seismic waves. For this purpose we compare the corrected *S*-wave polarigrams with the theoretical ones computed by different rupture models. We adopt a parametrization allowing us to associate an expected theoretical *S*-wave polarization with each fault portion: we divide the fault plane into 152 square subsources with a dimension of 1 km (that is, a little shorter than the smallest wavelength limited by the adopted frequency band) and located every kilometre along the fault strike direction at different depths. Each subsource starts to radiate when it is reached by the rupture front.

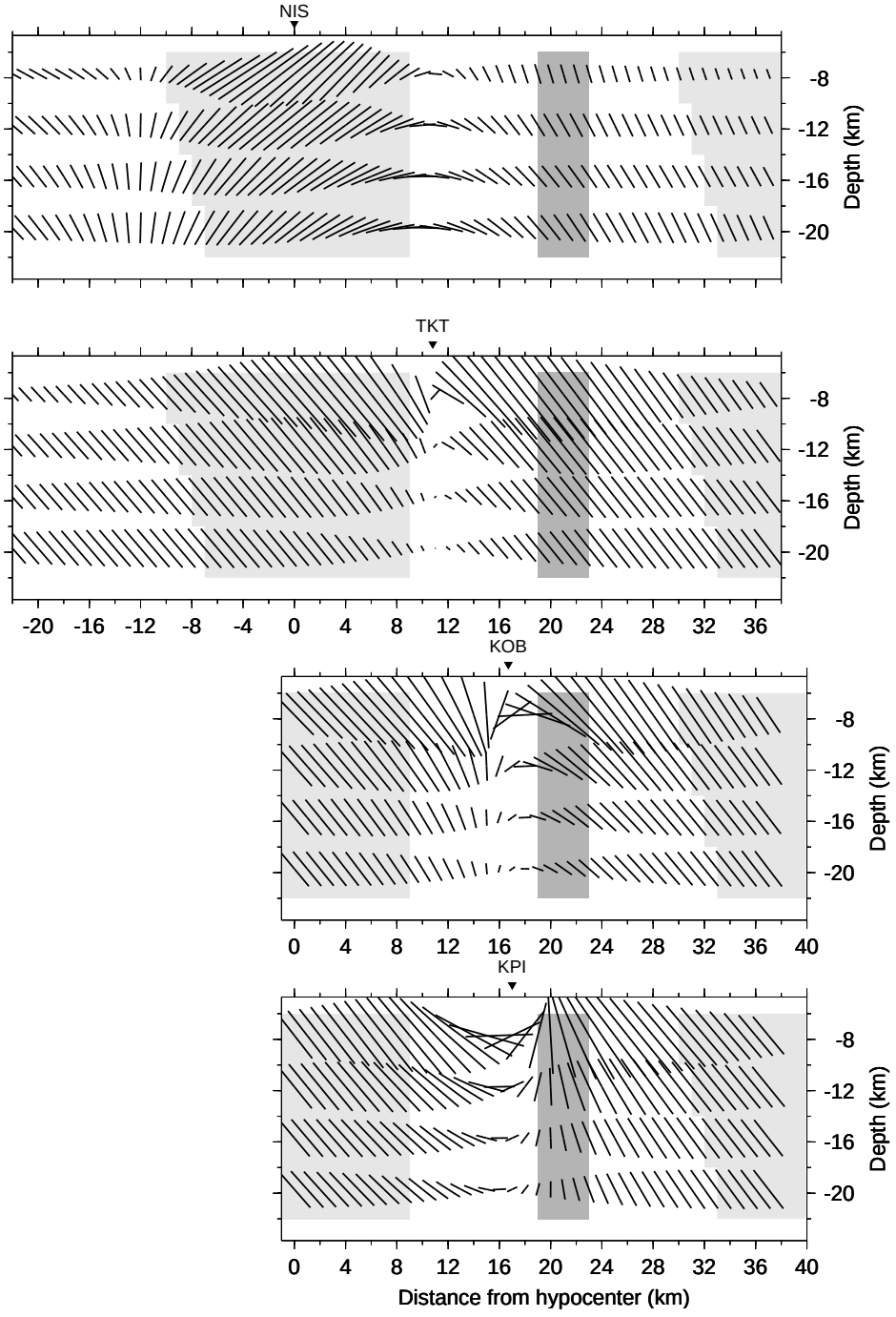

Figure 10. Theoretical *S*-wave polarization expected at the eight selected sites and calculated for a pure right-lateral mechanism (strike 231°, dip 85°W, rake 180°). The representation is the same as in Fig. 7. The shaded areas represent the allowed spatial domains constrained by the polarization (see text). In light grey we indicate those areas that radiate the stable *S*-wave polarization, while in dark grey we show the patches responsible for the N223°E and the N295°E polarized pulses at stations EKB and RKI (S_5 source).

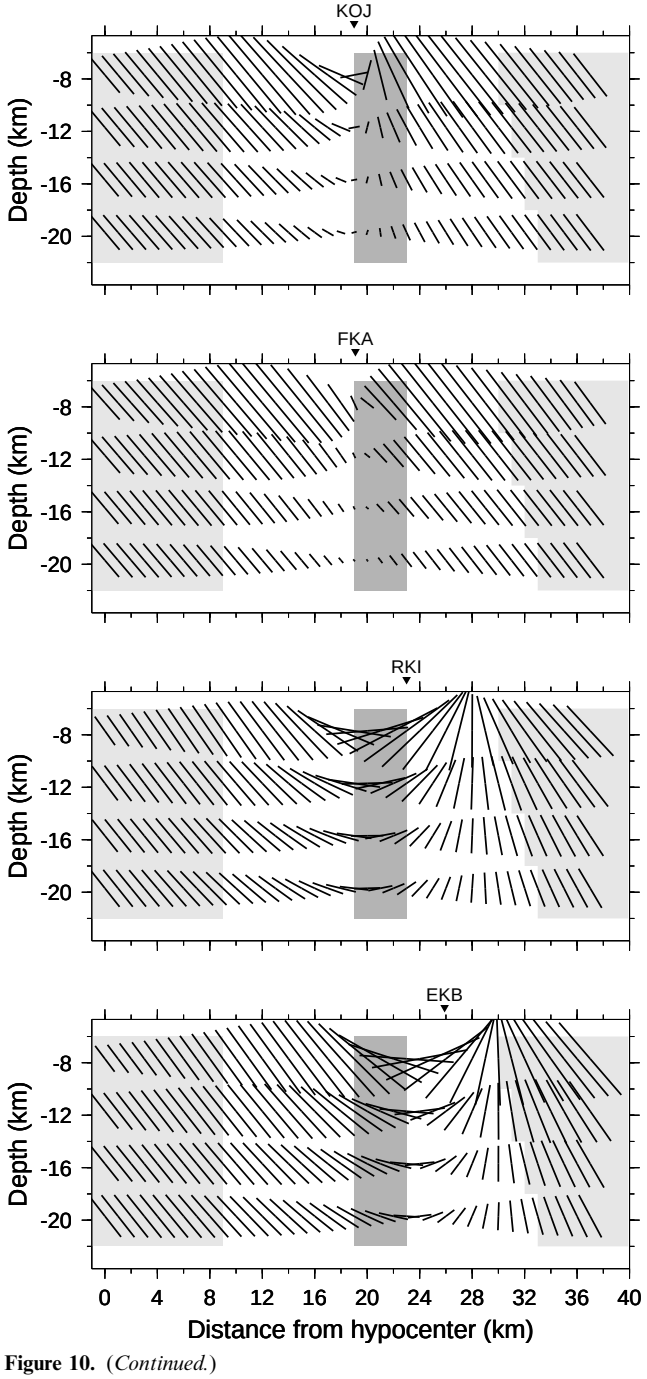

Figure 10. (*Continued.*)

In the first tentative model, we assume a constant rupture velocity and a uniform slip distribution on the fault plane. We use the fault geometry described in the previous section and we consider the three faulting mechanisms used in Fig. 9: a pure right-lateral strike-slip mechanism (fault parameters are: strike 231°; dip 85°; rake 180°), and two oblique mechanisms with 30 and 50 per cent reverse components (rake angles are 150° and 135°, respectively, following the convention of Aki & Richards 1980). We calculate the theoretical *S*-wave polarization vectors using the assumed rupture models. Note that we model the rupture history only on the Kobe fault system. Only for stations NIS and TKT (we do not use AWA in the present analysis because this site is not inside the *S*-wave window) do we extend the rupture for another 20 km in the direction of the Nojima fault, but with the same geometry as the Suma, Suwayama and Gosukebashi faults.

We assume that no slip occurred on the Kobe fault system at depths shallower than 8 km (Sekiguchi *et al.* 1996; Wald 1996; Yoshida *et al.* 1996). For this reason we distribute our subsources in a depth interval ranging between 8 and 20 km that agrees with the depth proposed by Kikuchi & Kanamori (1996) in their teleseismic modelling. We calculate the mean direction of polarization in the far-field approximation (ray theory), considering direct *S* waves only. We use the velocity structure proposed by Sekiguchi *et al.* (1996) for KBU, which can be considered as a reliable velocity model for rock sites. The use of different velocity models would yield source location errors smaller than the resolution allowed by the analyses performed in this study and presented in the following. For each mechanism considered here, Figs 10, 11 and 12 show the theoretical *S*-wave horizontal polarization direction at a selected recording site radiated by each subsource distributed along the strike on several line sources located at different depths.

The stability of *S*-wave polarization at most of the sites as well as the rotation of the polarization direction expected at sites RKI and EKB are consistent with the NE propagation of the rupture. For each faulting mechanism, we look for suitable domains on the fault plane that give a theoretical polarization in agreement (within $\pm 20°$) with the observed polarization at the stations considered. In other words, we identify those subsources that radiate a theoretical polarization that fits the polarization observed on the recorded data. Two areas of high-frequency radiation were identified: the first is controlled by the stable *S*-wave polarization oriented NNE–SSW at NIS and NNW–SSE at the other stations and is indicated by the light grey areas in Figs 10, 11 and 12; the second is constrained by the N223°E-oriented pulse at RKI and the N295°E-oriented pulse at EKB and is indicated by dark grey shading. As shown in these figures, when the rupture front has just passed RKI, EKB starts to be nodal and its *S*-wave polarization vector starts to rotate: this is clearly observed in the recorded data shown in Fig. 6. In the following we will refer to these two fault areas as the first and third subevents.

5.1 The third subevent

The temporal rotation of polarization observed at RKI and EKB allows us to pick the phase on the polarigrams (see Fig. 6 and Table 4); we named this phase S_5 (see below). The picking is made at the onset of the pulse. The accuracy of the picking is about 0.3 s, that is, the period of the oscillations around the central pick due to the zero-phase recursive filter used in this study.

For each slip direction considered, we can compute the rupture time of each subsource belonging to the fault domain constrained by the *S*-wave polarization using the estimated triggering times and the phase picking, and according to the following relation:

$$T_{S_i} + T_{S_0} = T_t + T_a - T_p\,, \tag{1}$$

where T_{S_0} is the origin time of the earthquake, T_t is the station trigger time, T_{S_i} is the rupture propagation time from S_0 to S_i, T_a is the arrival time delay of the S_i phase after the triggering, and T_p is the propagation time of the S_i phase.

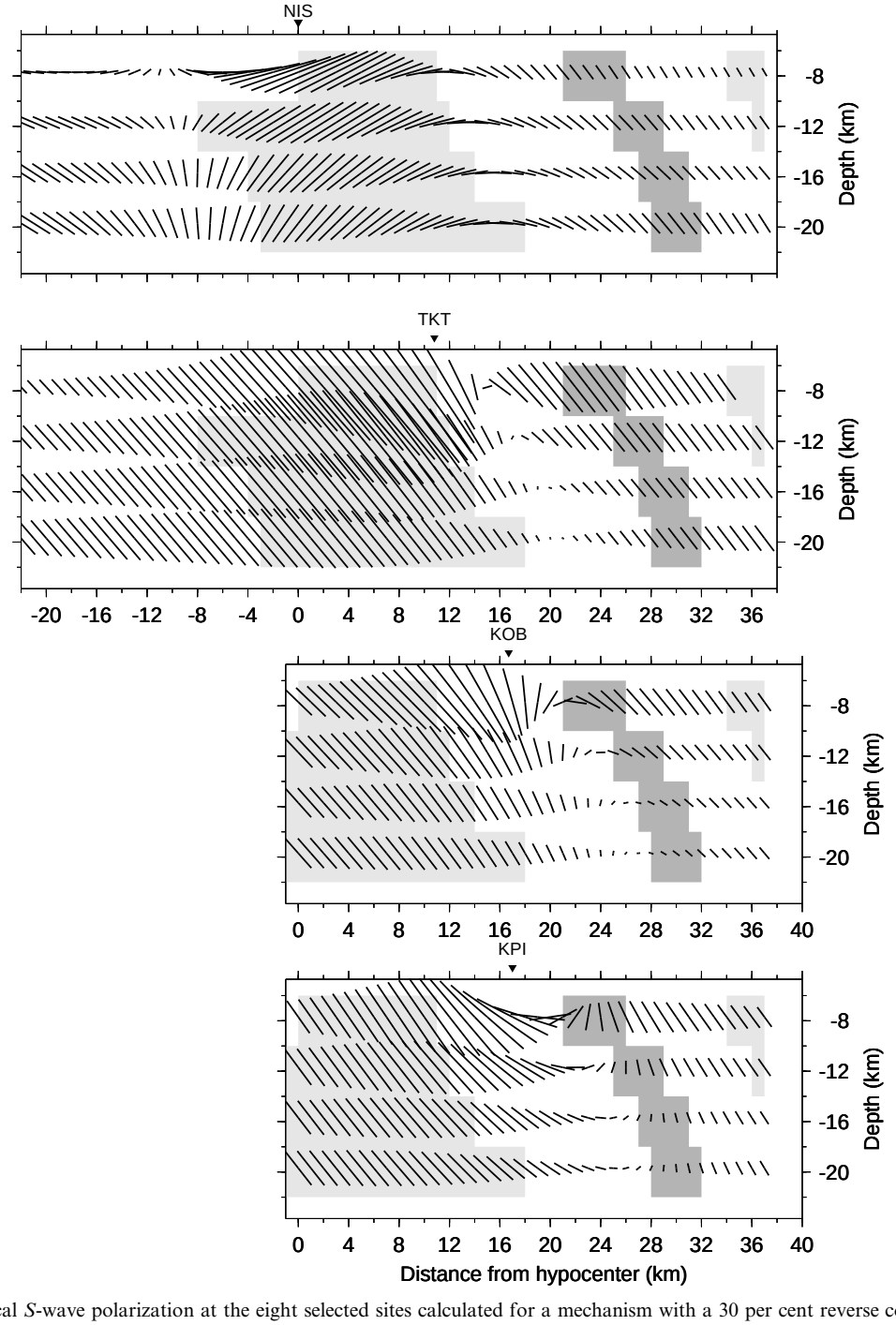

Figure 11. Theoretical *S*-wave polarization at the eight selected sites calculated for a mechanism with a 30 per cent reverse component of the slip vector (strike 231° dip 85°W, rake 150°). See Fig. 7 for explanations. The shaded areas have the same meaning as those in Fig. 10.

By using the arrival times of the S_5 phase at stations RKI and EKB in eq. 1 (see Fig. 6 and Table 4), we can define the space–time domain that allows us to fit both the polarization and the arrival times. Its position is shown as a labelled box in Fig. 13(a) for each of the three mechanisms considered in this study.

Let us first consider the pure right-lateral mechanism. The space–time diagram plotted in Fig. 13(a) (left panel) allows us to estimate a mean rupture velocity by connecting with straight lines the nucleation point (the origin of the diagram) to the centre and the edges of the S_5 subsource domain. The upper limit for the rupture velocity is the shear wave velocity at the corresponding depths (3.46 km s^{-1} between 5 and 18 km). It is indicated in Fig. 13(a) as a straight line labelled V_s. This figure shows that deeper S_5 subsources correspond to higher values of the rupture velocity. The resulting rupture velocities calculated for different depths of the S_5 source are listed in Table 5; they range between 2.34 and 3.15 km s^{-1}. Only subsources deeper than 16 km provide values of rupture velocity that agree with the values obtained in previous studies (see Wald 1996 and Sekiguchi *et al.* 1996 and the discussion therein).

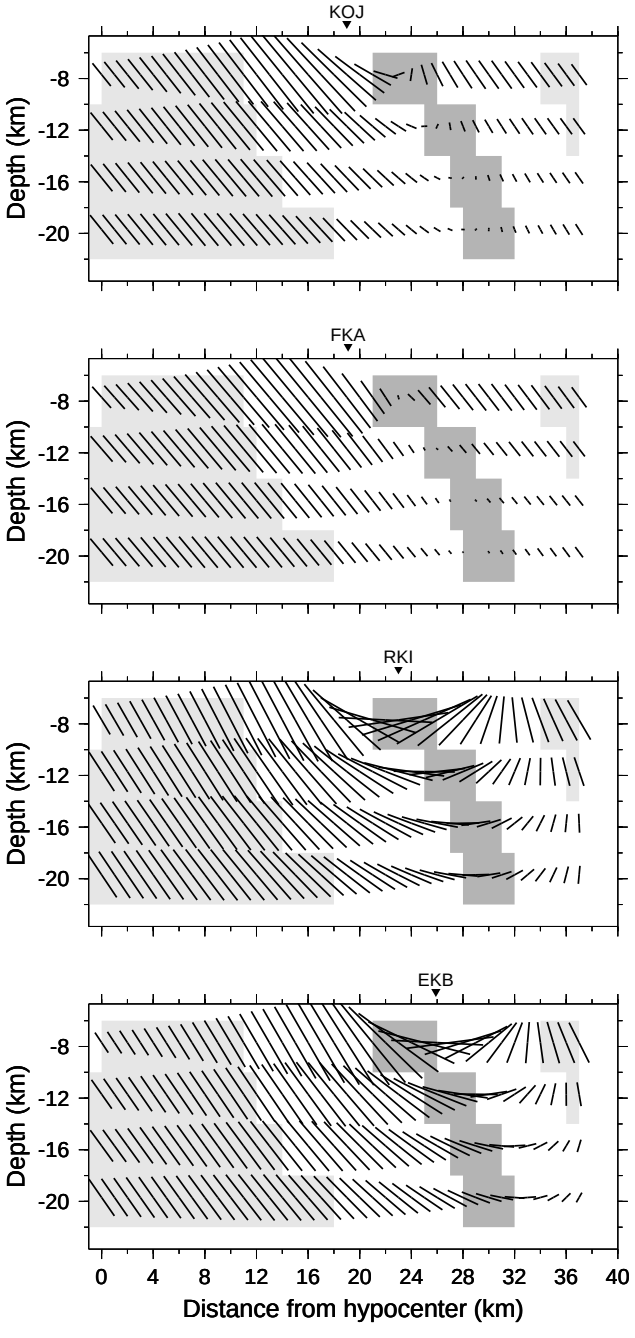

Figure 11. (*Continued.*)

For a given depth, knowledge of the mean rupture velocity yields a specific nucleation time, and hence a specific arrival time at the other stations. Using these arrival times, which are listed in Table 6, we verify that the modelled S_5 phase has to be energetic at stations EKB and RKI and nodal at all the other stations in order to fit the observed polarization data. According to the position of the S_5 source, Fig. 10 shows that a pure right-lateral mechanism predicts an energetic phase at RKI only for depths shallower than 12 km. This allows us to fix the S_5 source depth. The same figure shows that a right-lateral mechanism predicts a nearly nodal S_5 phase at FKA and KOJ only for depths greater than 8 km. However, in this depth range, the S_5 phase is clearly energetic at stations KOB and KPI and the resulting expected polarization at KPI does not fit the observed value. This means that our predictions do not agree with the observed polarigrams. Therefore, we conclude that a pure right-lateral faulting mechanism for the S_5 subsource is not compatible with the observations.

We therefore consider the two proposed oblique mechanisms. The domains allowed in the spatio-temporal diagram are plotted in Fig. 13(a), middle and right panels. As discussed in the previous section, increasing the reverse slip component modifies the *S*-wave radiation pattern and increases the vertical resolution (compare Fig. 10 and Figs 11 and 12, and Fig. 13(a) left, middle and right panels). These considerations have a big effect on the possible values of rupture velocity, as illustrated in Fig. 13(a). If we reject a super-shear rupture velocity, a rake angle of 150° needs a S_5 subsource located shallower than 16 km, while a rake angle of 135° requires a S_5 subsource depth shallower than 12 km. The resulting average rupture velocities for these two faulting mechanisms are listed in Table 5.

We have computed the arrival times of the S_5 subsources for the two mechanisms at all the stations; they are listed in Table 6. As illustrated in Fig. 11, a faulting mechanism with a 30 per cent reverse component (rake 150°) predicts a nodal phase at stations KOB, KPI, FKA and KOJ only when the S_5 subsources are located at depths ranging between 8 and 16 km. The rupture model with a slip direction with a 50 per cent reverse component (rake 135°) predicts a nodal S_5 phase at all the stations considered (as is evident in Fig. 12) for subsources shallower than 12 km.

In order to avoid a super-shear rupture velocity and to radiate an energetic phase at RKI, KBU, SHI and MOT, a reverse component of slip requires a shallow depth for the S_5 source, although it has to be deeper than 8 km to avoid the S_5 phase becoming energetic at KPI and KOJ. Therefore, we conclude that a reverse component of the slip vector improves the fit to the data. This yields an average rupture velocity of between 2.65 (see Table 5) and 3.46 km s^{-1} (the upper limit is the shear wave velocity), thus defining an allowable domain for the main rupture velocity during faulting.

5.2 The first subevent

Now that we have constrained the slip direction and rupture velocity for the third subevent, we investigate the rupture mechanism during the first subevent. Because the observed *S*-wave polarization is stable for quite a long time window (see Fig. 6), it is difficult to pick the phases as we did for the S_5 subsources. Nevertheless, it is reasonable that all the phases having a constant *S*-wave polarization belong to the temporal domain of stability of the *S*-wave polarization vector, which we have identified for each polarigram (see light grey boxes in Fig. 6). In other words, the arrival times of these phases lie within an allowable time window that starts at the hypocentral arrival time and ends with the last well-polarized energetic pulse. TKT has the largest temporal domain of stability (larger duration of constant polarization). On the TKT polarigram, we carefully pick the end of the last well-polarized energetic pulse, named TKT_f (f for final) in Fig. 6 (see Table 4). Using the TKT hypocentral arrival time (see Table 3) and the TKT_f phase arrival time (see Table 4), eq. (1) provides an allowable space–time domain for the area that radiates a stable polarization. For each mechanism considered here, we have plotted in Fig. 13(b) the position of this domain for several depths (left panel for the pure right-lateral mechanism, middle and right

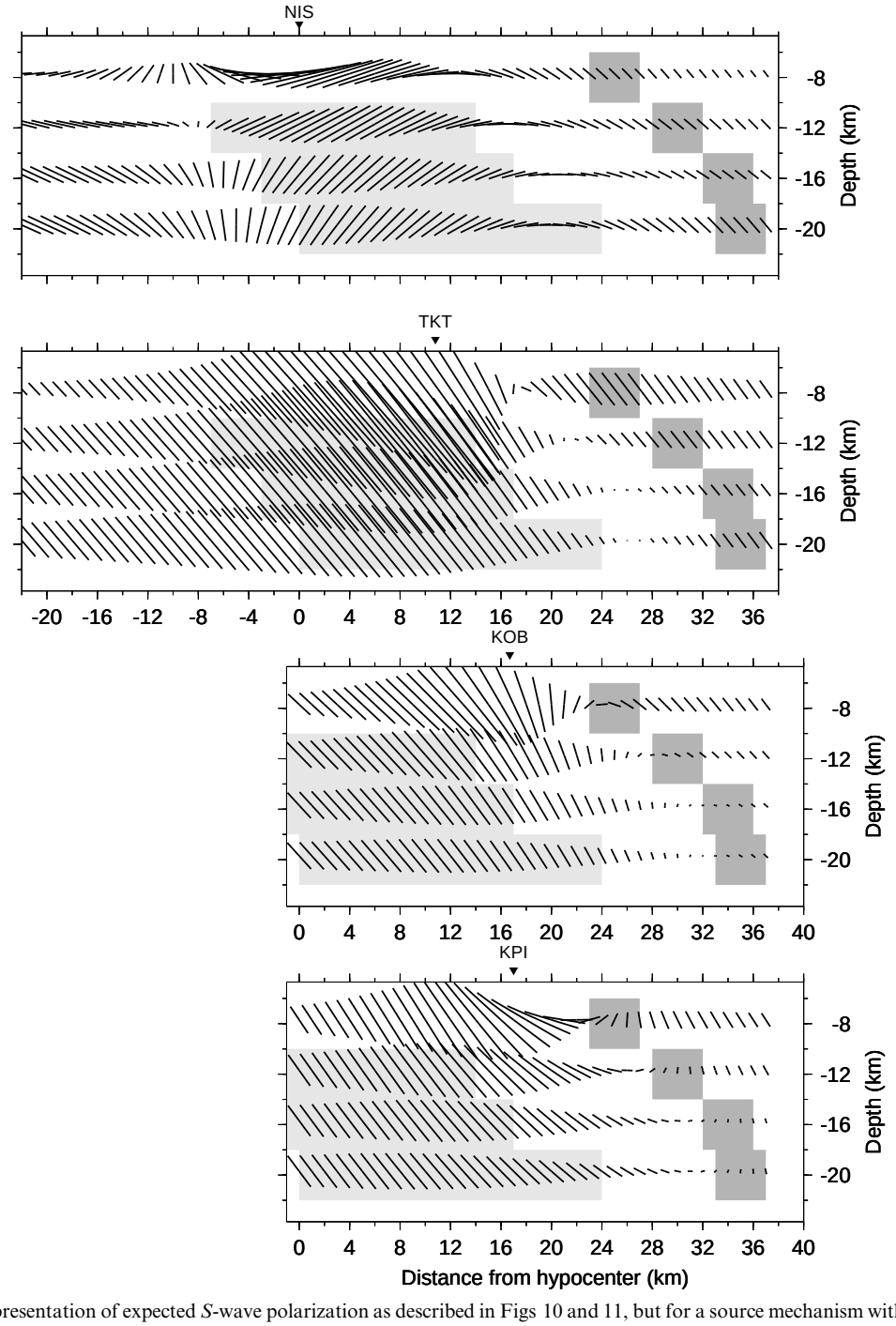

Figure 12. Same representation of expected *S*-wave polarization as described in Figs 10 and 11, but for a source mechanism with a 50 per cent reverse component of the slip vector (strike 231°, dip 85W°, rake 135°). See Fig. 7 for explanations. The shaded areas have the same meaning as those in Fig. 10.

panels for the two oblique mechanisms). We assume a constant rupture velocity within the allowable interval defined above and indicated by the shaded zone in Fig. 13(b); this figure also shows the spatio-temporal domains for different depths for the rupture mechanisms investigated here. Any straight line lying within the shaded triangle can provide a set of subsources that fit both the polarization and the arrival time distribution to the sites considered.

Fig. 13(b) shows that a pure right-lateral mechanism for the subsources belonging to the first subevent is not compatible with the assumption of a constant rupture velocity. In fact, under this assumption the only possibility for fitting the direction and the duration of the stable polarization at all sites is to assume a very low rupture velocity. For instance, if the subsources are located at 20 km depth, the resulting rupture velocity is 1.7 ± 0.36 km s^{-1} (50 per cent of the shear wave velocity). Moreover, in order to fit the arrival times of the phases radiated by the S_5 source, the rupture has to propagate from the first to the third subevent (S_5 subsource) at a super-shear rupture velocity (see Fig. 13b).

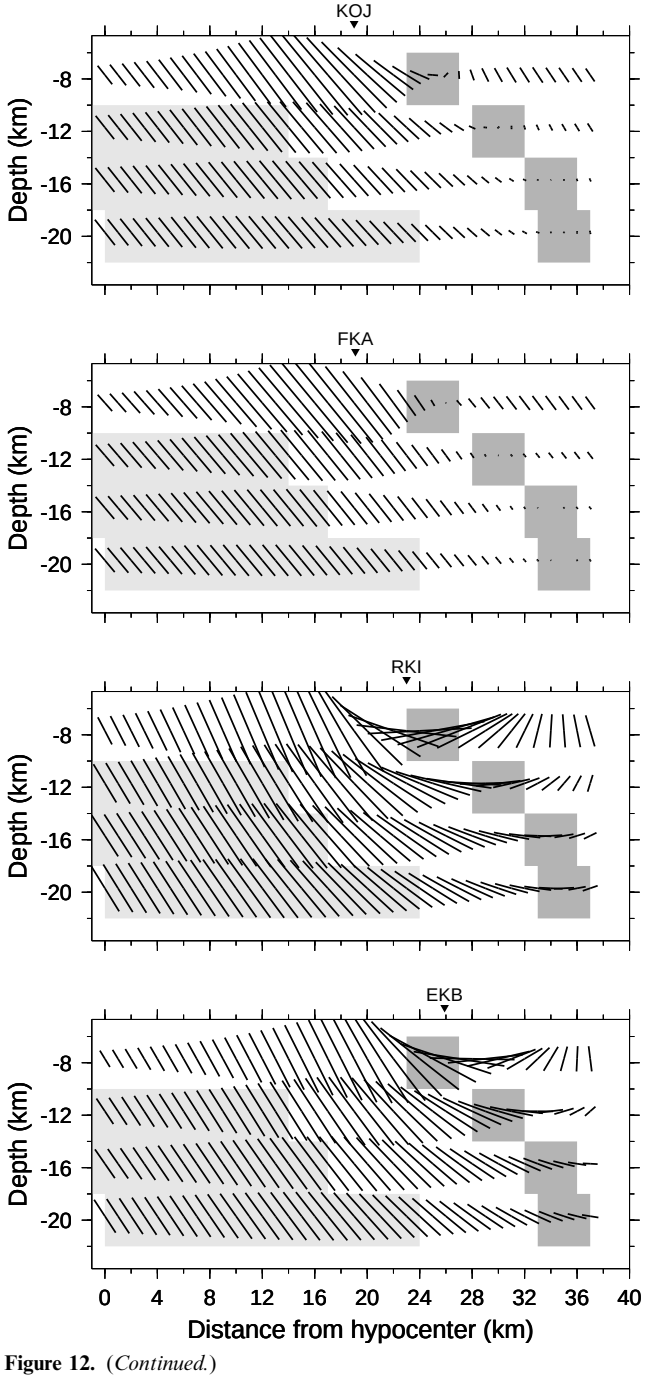

Figure 12. (*Continued.*)

In this discussion we have implicitly assumed that the rupture mostly propagated along the strike direction of the fault. It might be suggested that, immediately after nucleation, the rupture propagated up-dip and only afterwards along the strike direction. To shed light on this hypothesis we plot in Fig. 13(c) a space–time diagram where we show the depth and the rupture time of those subsources that radiate the proper polarization for the first subevent at all of the stations. The straight line labelled V_s stands for the shear wave velocity (centred on the nucleation point). The line labelled V_r represents the highest possible rupture velocity that, assuming an up-dip rupture propagation, allows us to fit the duration of the stable polarization at TKT. Its value is 1.42 km s^{-1} ($\pm$0.36 km s^{-1}), that is 41 per cent of the shear velocity. Also, in this case the moving rupture front should propagate from the first to the third subevent (S_5 subsource) at a super-shear velocity. In summary, we conclude that a pure right-lateral mechanism during the first subevent should require very complex rupture scenarios with unusually low rupture velocities.

On the other hand, the oblique faulting mechanisms provide clear evidence for NE rupture propagation (along the strike direction of the fault) in agreement with the isochrone distribution presented in Fig. 7. As shown in Fig. 13(b), middle panel, for the model with a 30 per cent reverse component (rake 150°), the subsources located at depths equal to or deeper than 16 km are compatible with the hypothesis of a nearly constant rupture velocity, whatever the velocity is within the allowable range. For the source model with a 50 per cent reverse component (rake 135°), only the sources located at 16 km depth are compatible with this hypothesis for a rupture velocity lower than or equal to 3.0 km s^{-1} (see Fig. 13b, right panel).

6 DISCUSSION

The analysis of *S*-wave polarization presented in this study allows us to extract the main features of the high-frequency rupture process during the 1995 Hyogo-ken Nanbu (Kobe) earthquake. The set of possible source models that provide an acceptable fit to the observed polarigrams is summarized in Fig. 13. The trade-off between the source parameters we have constrained (slip direction, rupture velocity and subevent positions) is also clearly seen in this figure.

We have shown that most of the complexity of the observed strong-motion waveforms (*S* waves) is due to anisotropic effects. The anisotropy parameters obtained in this study reflect the tectonic framework of the Kobe area. The polarization correction is consistent with the presence of hexagonal anisotropy with a horizontal symmetry axis in the sediments. Far from the causative faults the fast *S*-wave polarization is oriented E–W, parallel to the regional compressive stress field. Close to the causative faults the fast *S*-wave polarization is oriented nearly parallel to the fault strike. The resulting anisotropy parameters are consistent with those obtained from analysis of the aftershocks recorded on temporary stations (see Tadokoro *et al.* 1999). This strongly supports the validity of the anisotropy characteristic we have estimated for the selected sites.

The correction for crustal anisotropy yields coherent time histories at most of the selected recording sites. We noticed two main features on the corrected polarigrams: the stability of the *S*-wave polarization vector for most of the *S*-wave duration ($\sim$5 s; see the light grey shaded area in Fig. 6), and the evident time variation of the *S*-wave polarization vector on the polarigrams at EKB and RKI (see the dark grey shaded area in Fig. 6). This allows us to constrain the space and time locations of two high-frequency subevents.

According to our results, the first subevent, located near the hypocentre, is deeper than 16 km and extends up to nearly 15 km along the strike direction. The third subevent on the Kobe fault system is shallower (its depth ranges between 10 and 14 km) and it is located between 24 and 30 km from the hypocentre along the strike direction. We exclude a pure right-lateral mechanism (rake angle 180°) for both subevents in the Kobe area (i.e. the Suma–Suwayama–Gosukebashi faults). Fig. 13 shows that a pure right-lateral mechanism for the first subevent would require either a NE or an up-dip rupture

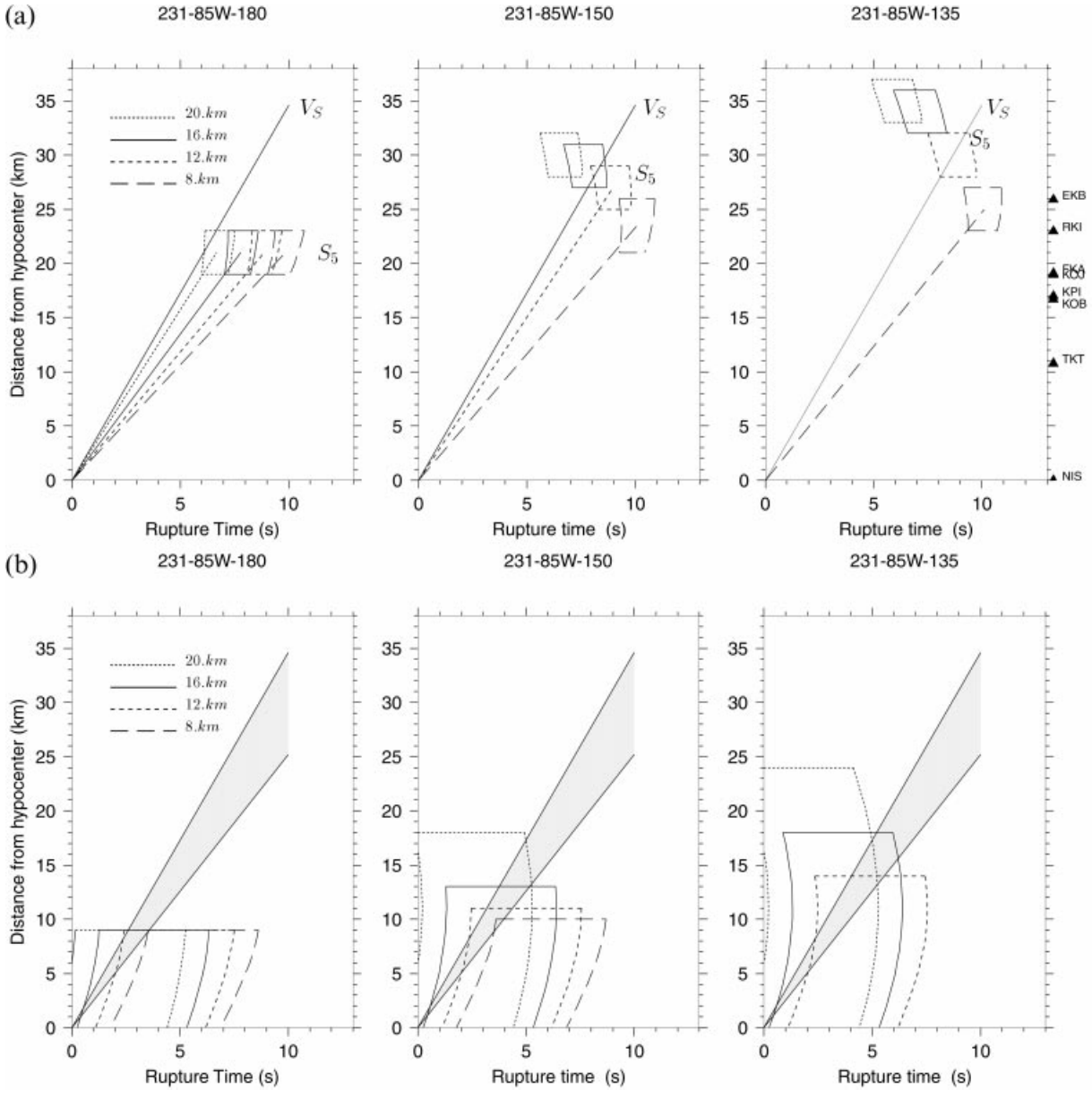

Figure 13. (a) Third subsource. Spatio-temporal diagrams for the three different source models (left panel: a pure right-lateral mechanism; middle panel: mechanism with a 30 per cent reverse component of slip; right panel: mechanism with a 50 per cent reverse component) showing the positions along the fault strike of the subsources (for different depths) that radiated the proper *S*-wave polarization observed at the selected sites with the appropriate arrival time. The line labelled V_s indicates a rupture velocity equal to the shear wave velocity. The other lines indicate the mean rupture velocities deduced from the position of the S_5 source as mentioned in the text and reported in Table 6. (b) First subsource. The boxes represent the allowable space–time domains at different depths for the subsources belonging to the first subevent and for the three source mechanisms considered in this study (same representation as in a). The shaded cone represents the domain of possible mean rupture velocities deduced from our analysis (see text). (c) Spatio-temporal diagram for an up-dip rupture propagation during the first subevent (the beginning of earthquake rupture). We show the position along the up-dip direction of the fault of the subsources that radiate the appropriate *S*-wave polarization observed at the sites considered with the appropriate arrival times. The box represents the allowable depth–time domain for the set of subsources belonging to the first subevent. The line labelled V_s indicates a rupture velocity equal to the shear wave velocity; the line labelled V_r indicates the highest possible rupture velocity assuming an up-dip rupture propagation hypothesis. The star represents the hypocentre.

propagation at an unusually low rupture velocity. For both such possibilities, the acceleration of the rupture front after the first subevent should imply a super-shear rupture velocity. On the other hand, an oblique faulting mechanism for the first subevent is compatible with the hypothesis of a nearly constant rupture velocity (whatever the velocity is within the allowable range) and yields a simple rupture history.

We also confirm an oblique mechanism with a slip direction ranging between 150° and 135° for the third subevent. For the first model (30 per cent reverse component) S_5 is located at a depth of 12 km, yielding a mean rupture velocity equal to 2.95 ± 0.36 km s^{-1}, i.e. 85 per cent of the shear velocity (see Fig. 13a, middle panel, and Table 5). The second model (50 per cent reverse component) S_5 subsource has to be shallower

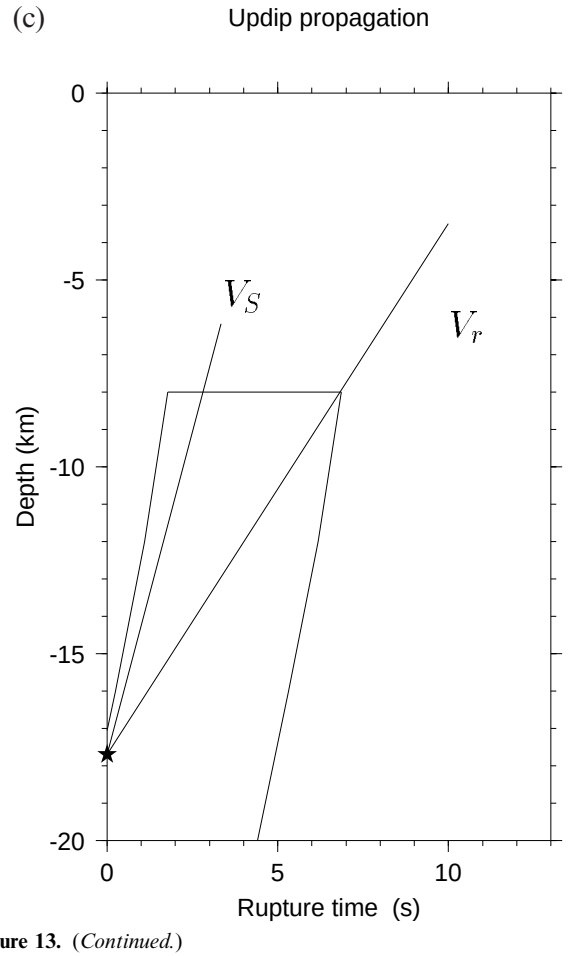

Figure 13. (*Continued.*)

than 16 km. Two average rupture velocities are possible, corresponding to different source depths: if S_5 is located at 12 km, the rupture velocity is equal to the shear velocity, while for S_5 located at 8 km, the rupture velocity is equal to 2.65 ± 0.36 km s^{-1}, i.e. 76 per cent of the shear velocity (see Fig. 13a, right panel, and Table 5). The possibility of distinguishing between 30 and 50 per cent reverse components (between rake values of 150° and 135°) is beyond the resolution of the *S*-wave polarization analysis we have performed in the present study. We emphasize that the range of possible values for the source parameters investigated in this study guarantees a fit to the data.

The spatial extent of the two subevents investigated in this study as well as their position on the fault plane agrees with the large-scale features of the faulting deduced by strong-motion waveform inversions performed by Wald (1996) and Yoshida *et al.* (1996) at lower frequencies. There are some differences between our model and the models resulting from the combined inversions presented by these authors, in particular for the third subevent location. This could suggest that geodetic and teleseismic data do not constrain the third subevent well, only the first one. One possible explanation may be the difference in the frequency band used: it might be possible that the third subevent released most of its energy at high frequencies.

Our suggested values for the rupture velocity agree with those proposed by several other studies (Sekiguchi *et al.* 1996; Wald 1996; Yoshida *et al.* 1996). Wald (1996), for instance, tested different values of rupture velocity ranging between 2.5 and 3.2 km s^{-1}. He pointed out that, although rupture velocities higher than 2.8 km s^{-1} provide a marginally better fit to the data, the resulting slip patterns are less compatible with the slip pattern resulting from geodetic data. Yoshida *et al.* (1996) showed that an oblique mechanism for the first subevent is required by geodetic and teleseismic data.

Although an exhaustive exploration of the model space is beyond the goals of the present paper, we propose a rupture model that allows us to compare synthetic and observed polarigrams at the recording sites considered here. We assume a faulting mechanism with a 30 per cent reverse slip component (rake 150°), which implies that the first subevent is deeper than 16 km. To obtain a good fit to the polarigram resulting from the TKT recordings, we use a distribution of four subsources

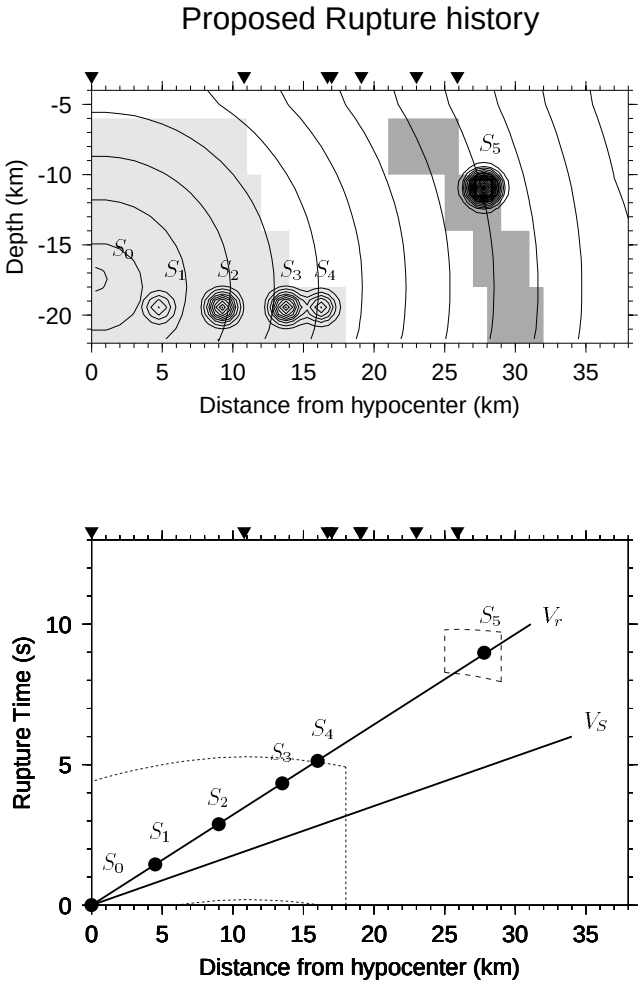

Figure 14. Proposed model for the rupture history of the 1995 Hyogo-ken Nanbu (Kobe) earthquake. We assume a uniform slip on a fault striking 231°, dipping 85°NW and with a rake angle of 150°. The rupture velocity is constant and equal to 3.1 km s^{-1} (see text). Top panel: proposed rupture model. The shaded areas represent the allowable spatial domains constrained by *S*-wave polarization of high-frequency radiation (see Fig. 11). We plot the position on the fault plane of the six subsources used to compute the synthetic polarigrams (see Table 7). Bottom panel: spatio-temporal diagrams for the different high-frequency radiation sources used in this model. The constant rupture velocity (3.1 km s^{-1}) is represented as a line labelled V_r. The circles distributed along this line are the six subsources used in the modelling. The solid triangles represent the projection of the selected stations on the fault plane (respectively from left to right: NIS, TKT, KOB and KPI, FKA and KOJ, RKI and EKB).

all belonging to the first subevent and located at nearly 20 km depth (see Fig. 14). We locate the S_5 source 28 km NE of the hypocentre at a depth of 11 km. This location guarantees the best fit to the *S*-wave polarization observed at RKI and EKB. This constrains the rupture velocity to be 3.1 km s^{-1} in our model. We use a Gaussian distribution of slip centred in a squared subsource whose width and length are equal to 4 km. To obtain a better scaling of the relative amplitudes of the *S*-wave pulses in time, we assign a different weight to each subsource (see Table 7). The final proposed source model is summarized in Fig. 14.

Fig. 15 a shows the comparison between the observed (above) and the synthetic (below) polarigrams in the 0.6–2.0 Hz frequency band computed from the source model shown in Fig. 14. The time histories simulated at stations TKT, FKA and KPI show some discrepancies with the observed polarigrams. They are related to the uncertainty we have on the location of the sources belonging to the first domain. However, despite these small discrepancies, the time evolution of the *S* polarization is very well fitted at all of the sites by this simple rupture model.

For stations KBU, SHI and MOT (excluded from our investigation), absolute trigger times were available. As shown in Figs 2 and 7, these stations cover the same portion of the fault as EKB and RKI. Therefore, the S_5 phase has to be energetic at KBU, SHI and MOT. Modelling results are shown in Fig. 15(b); the theoretical S_5 phase is correlated in time with an energetic arrival clearly visible on the observed polarigrams confirming *a posteriori* that in our analysis the S_5 source is well constrained. As a further validation, in Fig. 15(c) we show the comparison between the synthetic and the observed polarigrams resulting from the borehole recordings at KPI and EKB. Borehole data are less affected by the non-linear effects that reduce the high-frequency amplitudes. As shown in this figure, the fit to the data resulting from borehole recordings is

Table 7. Sources used for the final modelling.

Source	Location* (km)	Depth (km)	Weight
S_0	0.0	17.7	2
S_1	4.5	20.0	4
S_2	9.0	20.0	10
S_3	13.5	20.0	10
S_3	16.0	20.0	6
S_5	28.0	11.7	20

*Location: distance NE from the hypocentre

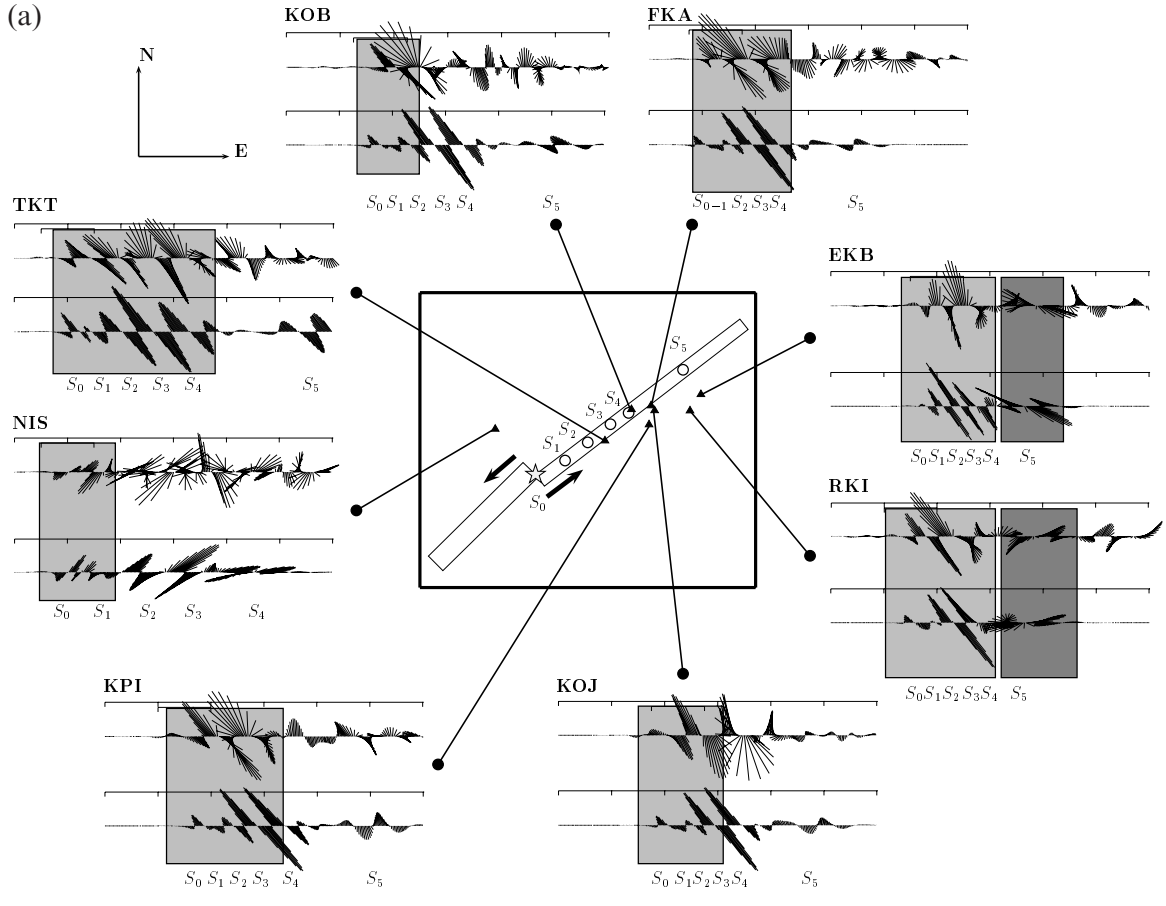

Figure 15. (a) Comparison between observed (top) and synthetic (bottom) polarigrams computed using the source model shown in Fig. 14. We use the same time window as shown in Fig. 6. We indicate the positions of the six subsources along the strike direction. The star shows the hypocentre location and the arrows indicate the direction of rupture propagation. (b) Comparison between observed (top) and synthetic (bottom) polarigrams computed using the source model shown in Fig. 14 for the three sites we did not consider in the previous analyses. The time window is plotted between 6 and 18 s. (c) Comparison between observed (top) and synthetic (bottom) polarigrams computed using the source model shown in Fig. 14 for the borehole recordings at KPI and EKB. We use the same time window as shown in Fig. 6.

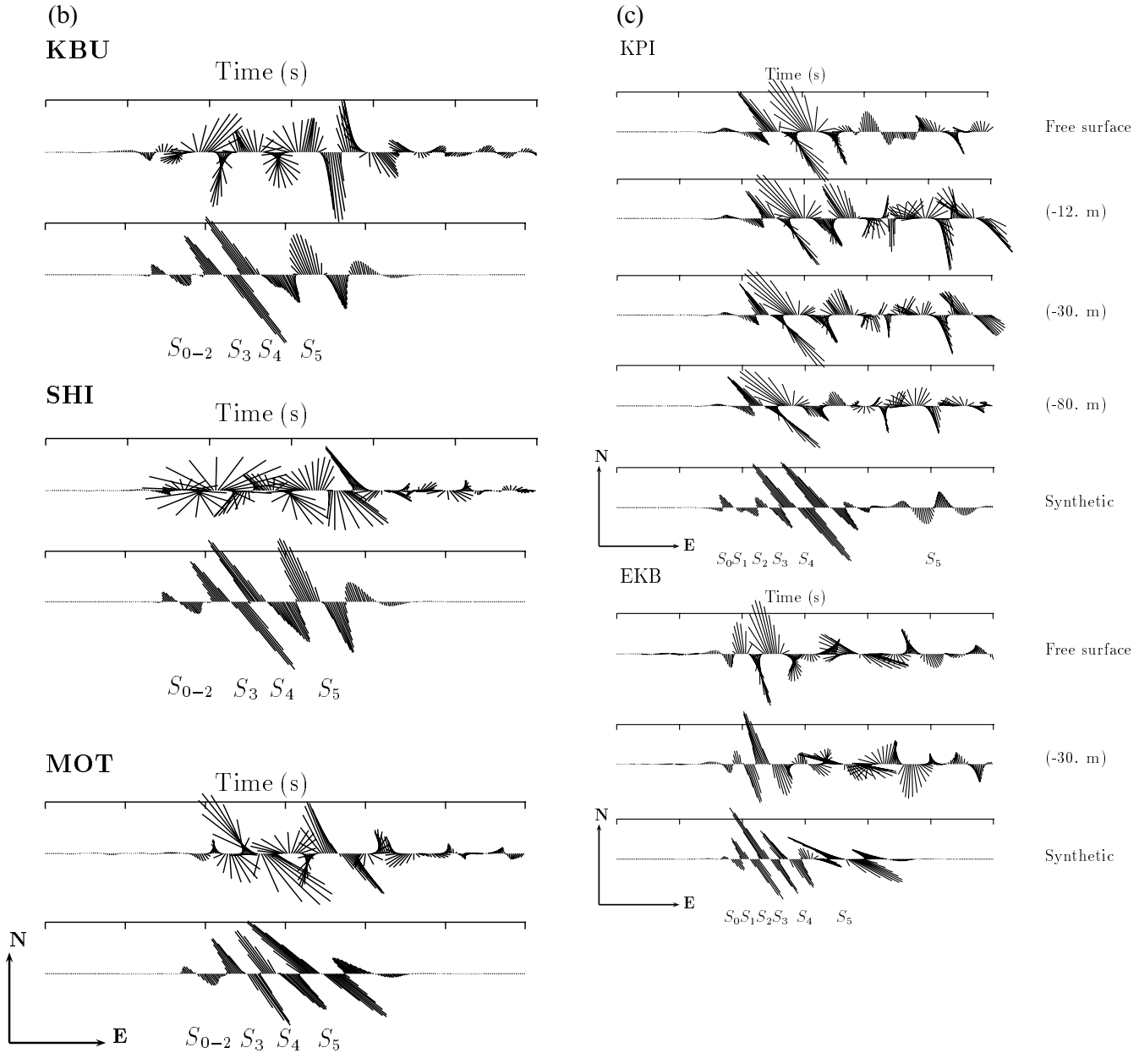

Figure 15. (*Continued.*)

improved with respect to the waveforms recorded at the Earth's surface; this is particularly evident for site EKB, where the S_5 phase, clear and energetic on the borehole recordings (EKD), is modelled well by our model.

Although the assumption of a constant rupture velocity as well as a constant slip direction during faulting might not be correct and more complex models can be proposed, we emphasize that a very simple model can explain the corrected *S*-wave polarization recorded during the 1995 Hyogo-ken Nanbu (Kobe) earthquake.

7 CONCLUSIONS

The present work shows that *S*-wave polarization analysis is a powerful tool to constrain source parameters such as slip direction and rupture velocity that are weakly resolved by waveform inversion procedures. Guatteri & Cocco (1996) have discussed the uncertainties in constraining the slip direction for the 1989 Loma Prieta earthquake by modelling near-source ground motions. Our study of the 1995 Kobe earthquake confirms these results and points out the difficulties in determining both the rupture velocity and the subevent locations for large-magnitude earthquakes. We demonstrated that the proposed methodology has the advantage that it is also applicable when (non-linear) site effects (see Figs 3 and 15c) may have modified the observed amplitudes.

We emphasize that polarization analysis can be very useful for restricting the number of reliable starting models for iterative inversion procedures. High-frequency subsources can be located with a good resolution (1–2 km) and the allowable

variability of rupture velocity can be determined depending on the distribution of the recording sites and the selected distance and frequency ranges. However, the distance and frequency ranges for such analyses must be carefully selected and the effect of anisotropy in the upper crust must be taken into account.

ACKNOWLEDGMENTS

We wish to thank the following Japanese institutions for providing strong-motion recordings: the Committee of Earthquake Observation and Research in the Kansai Area (CEORKA), the Japan Meteorological Agency (JMA), Kansai Electricity Power Co. Inc., the Port and Harbor Research Institute, the Japan Railway Institute, Sekisui House Co. Inc., the Public Works Research Institute Ministry of Construction, Osaka Gas and Kobe city. M-PB is grateful to ING for supporting her in Rome, which motivated this collaboration. This research was supported by research funds of the Istituto Nazionale di Geofisica and of the Department of Earth Sciences of Oxford University. We appreciate the constructive reviews by an anonymous reviewer and Raúl Madariaga. This is IPGP contribution 1663.

REFERENCES

Aguirre, J. & Irikura, K., 1995. Preliminary analysis of non linear site effects at Port Island Vertical Array station during the 1995 Hyogo-Ken Nanbu earthquake at Higashinada Ward, Kobe city, *J. nat. Disast. Sci.,* **16-2,** 49–52.

Aki, K., Richards, P., 1980. *Quantitative Seismology, Theory and Methods,* W. H. Freeman, San Francisco, CA.

Bernard, P. & Madariaga, R., 1984. A new asymptotic method for the modeling of near-field accelerograms, *Bull. seism. Soc. Am.,* **74,** 539–559.

Bernard, P. & Zollo, A., 1989. Inversion of near-source S polarization for parameters of double-couple point like sources, *Bull. seism. Soc. Am.,* **79,** 1779–1809.

Beroza, G.C., 1991. Near-source modeling of the Loma Prieta earthquake: evidence for heterogeneous slip and implications for earthquake hazard, *Bull. seism. Soc. Am.,* **94,** 1631–1621.

Booth, D.C. & Crampin, S., 1985. Shear wave polarization on a curved wave front at an anisotropic free surface, *Geophys. J. R. astr. Soc.,* **83,** 31–45.

Bouin, M.-P. & Bernard, P., 1994. Analysis of strong-motion S wave polarization of the 15 October 1979 Imperial Valley earthquake, *Bull. seism. Soc. Am.,* **84,** 1770–1785.

Bouin, M.-P., Téllez, J. & Bernard, P., 1996. Seismic anisotropy around the Gulf of Corinth (Greece) deduced from three-component seismograms of local earthquakes and its relationship with crustal strain, *J. geophys. Res.,* **101,** 5795–5811.

Bowman, J.R. & Ando, M., 1987. Shear-wave splitting in the upper mantle wedge above the Tonga subduction zone, *Geophys. J. R. astr. Soc.,* **88,** 25–41.

Capuano, P., Zollo, A. & Singh, S.K., 1994. Source characteristics of moderate size events using empirical Green's function: an application to some Guerrero (Mexico) subduction zone earthquakes, *Ann. Geofis.,* **37,** 1659–1679.

Cocco, M. & Pacor, F., 1993. The rupture process of the 1980 Irpinia, Italy, earthquake from the inversion of strong motion waveforms, *Tectonophysics,* **218,** 157–177.

Cocco, M., Pacheco, J., Singh, S.K. & Courboulex, F., 1997. The Zihuatanejo, Mexico, earthquake of 1994 December 10 ($M=6.6$): source characteristics and tectonic implications, *Geophys. J. Int.,* **131,** 135–145.

Cohee, B.P. & Beroza, G.C., 1994. Slip distribution of the 1992 Landers Earthquake and its implications for earthquake source mechanics, *Bull. seism. Soc. Am.,* **84,** 692–712.

Crampin, S., 1987. Evaluation of anisotropy by shear wave splitting, *Geophys. J.,* **50,** 159–170.

De Chabalier, J.-B., Lyon-Caen, H., Zollo, A., Deschamps, A., Bernard, P. & Hatzfeld, D., 1992. A detailed analysis of microearthquakes in western Crete from digital three-component seismograms, *Geophys. J. Int.,* **110,** 347–360.

Evans, J.R., Julian, B.R., Foulger, G.R. & Ross, A., 1995. Shear wave splitting from local earthquakes at the Geysers geothermal fields, California, *Geophys. Res. Lett.,* **22,** 501–504.

Farra, V., Bernard, P. & Madariaga, R., 1986. Fast near source evaluation of strong motion for complex source models, in *Earthquake Source Mechanics, Maurice Ewing Series,* 6, pp. 121–130, eds Simpson, D.W. & Richards, P.G., AGU, Washington, DC.

Gledhill, K.R., 1991. Evidence for shallow and pervasive seismic anisotropy in the Wellington Region, New Zealand, *J. geophys. Res.,* **96,** 21 503–21 516.

Guatteri, M. & Cocco, M., 1996. On the variation of slip direction during earthquake rupture: supporting and conflicting evidence from the 1989 Loma Prieta Earthquake, *Bull. seism. Soc. Am.,* **86,** 1935–1941.

Hashimoto, M., Sagiya, T., Tsuji, H., Hatanaka, Y. & Tada, T., 1996. Co-seismic displacements of the 1995 Hyogo-ken Nanbu earthquake, *J. phys. Earth,* **44,** 255–280.

Hirata, K., *et al.*, 1996. Urgent joint observation of the aftershocks of the 1995 Hyogo-ken Nanbu earthquake, *J. phys. Earth,* **44,** 317–328.

Horikawa, H., Hirahara, K., Umeda, Y., Hashimoto, M. & Kusano, F., 1996. Simultaneous inversion of geodetic and strong-motion data for the source process of the Hyogo-ken Nanbu, Japan, earthquake, *J. phys. Earth,* **44,** 455–471.

Huzita, K. & Kazama, T., 1983. *Geology of the Kobe district, Quadrangle Series Scale 1:50 000, Geological Survey of Japan,* Tsukuba (in Japanese).

Ide, S. & Takeo, M., 1996. Source model of the Hyogo-ken Nanbu earthquake determined by near field strong motion records, *J. phys. Earth,* **44,** 649–655.

Irikura, K., Iwata, T., Sekiguchi, H., Pitarka, A. & Kamae, K., 1996. Lesson from the 1995 Hyogo-Ken Nanbu Earthquake: why were such destructive motions generated to buildings? *J. nat. Disast. Sci.,* **17,** 99–127.

Kagawa, T., Irikura, K. & Yokoi, I., 1996. Restoring clipped records of near-field strong motion during the 1995 Hyogo-ken Nanbu (Kobe), Japan, earthquake, *J. nat. Disast. Sci.,* **18,** 43–57.

Kakehi, Y., Irikura, K. & Hoshiba, M., 1996. Estimation of high frequency wave radiation areas on the fault plane of the 1995 Hyogo-ken Nanbu earthquake by the envelope inversion of acceleration seismograms, *J. phys. Earth,* **44,** 505–517.

Kaneshima, S., 1990. Origin of crustal anisotropy: shear wave splitting studies in Japan, *J. geophys. Res.,* **95,** 11 121–11 133.

Kikuchi, M. & Kanamori, H., 1996. Rupture process of the Kobe, Japan, earthquake of Jan. 17, 1995, determined from teleseismic body waves, *J. phys. Earth,* **44,** 428–436.

Nakamura, M. & Ando, M., 1996. Aftershock distribution of the 1995 Hyogo-ken Nanbu earthquake determined by the JHD method, *J. phys. Earth,* **44,** 329–336.

Nakamura, Y., 1995. Report of the 1995 Hyogo-ken Nanbu earthquake, *JR Earthquake Information,* Railway Technical Research Institute, Tokyo.

Nakamura, Y., Uehan, F. & Inoue, H., 1996. Waveform and its analysis of the 1995 Hyogo-ken Nanbu earthquake (II), *JR Earthquake Information,* Railway Technical Research Institute, Tokyo (in Japanese).

Nakata, T. & Yomogida, K., 1995. Surface fault characteristics of the 1995 Hyogo-ken Nanbu earthquake, *J. nat. Disast. Sci.,* **16,** 31–37.

Nemoto, H., Negishi, H. & Irikura, K., 1997. Re-examination of the hypocenter of the 1995 Hyogo-ken Nanbu earthquake, *Zisin2,* **50,** 125–129 (in Japanese with English abstract).

Nuttli, O., 1961. The effect of the earth's surface on the S-wave particle motion, *Bull. seism. Soc. Am.,* **44,** 237–246.

Savage, M.K., Peppin, W.A. & Vetter, U.R., 1990. Shear wave anisotropy and stress direction in and near Long Valley caldera, California, 1979–1988, *J. geophys. Res.,* **95,** 11 165–11 177.

Sekiguchi, H., Irikura, K., Iwata, T., Kakehi, Y. & Hoshiba, M., 1996. Minute locating of faulting beneath Kobe and the waveform inversion of the source process during the 1995 Hyogo-ken Nanbu, Japan, earthquake using strong ground motion records, *J. phys. Earth,* **44,** 473–488.

Special Working Group of the 1995 Hyogo-ken Nanbu earthquake, 1996. *Report on Strong Motion Records of the 1995 Hyogo-ken Nanbu Earthquake,* Architectural Institute of Japan and Working Group of earthquake-resistant construction, Kinki branch of Architectural Institute of Japan.

Spudich, P. & Frazer, L.N., 1984. Use of ray theory to calculate high-frequency radiation from earthquake sources having spatially variable rupture velocity and stress drop, *Bull. seism. Soc. Am.,* **73,** 2061–2082.

Spudich, P. & Oppenheimer, D., 1986. Dense seismograph array observations of earthquake rupture dynamics, in *Earthquake Source mechanics, Ewing Symposium,* Vol. 6, pp. 285–296, eds Das, S., Boatwright, J. & Scholtz, S., AGU, Washington, DC.

Tadokoro, K., Ando, M. & Umeda, Y., 1999. S wave splitting in the aftershock region of the 1995 Hyogo-ken Nanbu earthquake, *J. geophys. Res.,* **104,** 981–991.

Wald, D.J., 1996. Slip history of the 1995 Kobe, Japan, earthquake determined from strong motion, teleseismic, and geodetic data, *J. phys. Earth,* **44,** 489–504.

Wald, D.J. & Heaton, T.H., 1994. Spatial and temporal distribution of slip for the 1992 Landers, California earthquake, *Bull. seism. Soc. Am.,* **84,** 668–691.

Wald, D.J., Heaton, T.H. & Helmberger, D.V., 1991. Rupture model of the 1989 Loma Prieta earthquake from the inversion of strong motion and teleseismic data, *Bull. seism. Soc. Am.,* **81,** 1540–1572.

Wald, D.J., Heaton, T.H. & Hudnut, K.W., 1996. The slip history of the 1994 Northridge, California, earthquake determined from strong ground motion, teleseismic, GPS, and leveling data, *Bull. seism. Soc. Am.,* **86,** S49–S70.

Yoshida, S., Kotseku, K., Shibazaki, B., Sagiya, T. & Yoshida, Y., 1996. Joint inversion of near- and far-field waveforms and geodetic data for the rupture process of the 1995 Kobe earthquake, *J. phys. Earth,* **44,** 437–445.

Zhang, Z. & Schwartz, S.Y., 1994. Seismic anisotropy in the shallow crust of the Loma Prieta segment of the San Andreas fault system, *J. geophys. Res.,* **99,** 9651–9661.

Zollo, A. & Bernard, P., 1989. S-wave polarization inversion of the 15 October 1979, 23:19 Imperial Valley aftershock: evidence for anisotropy and a simple source mechanism, *Geophys. Res. Lett.,* **16,** 1047–1050.

Zuniga, R., Castro, R.R. & Dominguez, T., 1995. Stress orientation and anisotropy based on shear-wave splitting observations in the Cerro Prieto Fault area, Baja California, Mexico, *Pure appl. Geophys.,* **144,** 39–57.